2012

Characterization, Stability, and Transport Through Defects in Graphene Nanoribbons

Sri Krishna Divya Pemmaraju
Wright State University

Characterization, stability, and transport through defects in graphene nanoribbons

A thesis submitted in partial fulfillment of
the requirements for the degree of
Master of Science in Engineering

By

SRI KRISHNA DIVYA PEMMARAJU

B.E., KONERU LAKSHMAIAH COLLEGE OF ENGINEERING, 2007-2011.

2012
WRIGHT STATE UNIVERSITY

SCHOOL OF GRADUATE STUDIES

January 11, 2013

I HEREBY RECOMMEND THAT THE THESIS PREPARED UNDER MY SUPERVISION BY Sri Krishna Divya Pemmaraju ENTITLED Characterization, Stability, and transport through defects in graphene nanoribbons BE ACCEPTED IN PARTIAL FULFILLMENT OF THE REQUIREMENTS FOR THE DEGREE OF Master of Science in Engineering.

_____

Amir.A.Farajian, Ph.D.
Thesis Director

_____

George P. G. Huang, Ph.D. Chair
Department of Mechanical and Materials Engineering

Committee on Final Examination

_____

Hong Huang, Ph.D.

_____

Sharmila Mukhopadhyay, Ph.D.

_____

Andrew Toming Hsu, Ph.D.
Dean, School of Graduate Studies

ABSTRACT

Sri Krishna Divya Pemmaraju. MS in Engineering, Department of Mechanical and Material Engineering, Wright State University, 2013.*Characterization, stability, and transport through defects in graphene nanoribbons*

Graphene nanoribbons (GNRs) constitute a new class of nanostructured materials with unique properties and significant potential for applications. During production of GNRs, defects are generally introduced within the lattice. Assessment of defects' stability and characterization of their effects on GNRs are therefore very important for predicting GNRs performance under realistic circumstances. Here we consider various possible defects, namely the ones caused by removal/addition of carbon atoms from/to the lattice as well as those caused by bond rotation/rearrangement. Our study is based on ab initio geometry optimization and electronic structure calculations. We determine which defects can be stable in graphene nanoflakes and/or GNRs, by calculating the corresponding vibration modes. We further investigate how the presence of defects would modify electronic transport through defected GNRs. Among the defects considered, only some turn out to be stable within the GNR lattice. Transport in presence of defects is generally less compared to the pristine case,

however, different defects cause different levels of conductance reduction. We also investigate the effects of a spin-polarized defect on transport characteristics.

TABLE OF CONTENTS

LIST OF FIGURES

LIST OF TABLES

ACKNOWLEDGMENT

First I would like to express my deepest gratitude to my advisor Dr. Amir A.Farajian for giving me a once in lifetime opportunity to be part of his elite research team and for guiding me at every step of my research. And I want to thank my advisor Dr.Amir A.Farajian for having confidence in my work abilities and for giving me the independence to explore the things in my own way.

I would like to thank my fellow teammates for their support and guidance. And, I would like to thank the committee members for their valuable suggestions and comments.

I would like to thank my family for the love and care and for encouraging me to pursue my dreams.

I would like to thank all my friends for their love and support. And, I would like to thank to all the teachers and Professors from my school till n for shaping me as a good student.

This research was supported by the National Science Foundation Grants ECCS-0925939 and STTR Phase II grant IIP-1057999.

DEDICATION

This dissertation is dedicated to my lovely parents

1. Introduction

1.1Graphene and its importance:

Carbon is the 4rth abundant element by mass in universe. Due to its flexibility in the crystal structure carbon has the ability to form different allotropes. The two main allotropes of carbon are diamond and graphite[1]. Diamond is well known for its excellent mechanical and optical properties. Graphite has sp^2 hybridization and it has weak van der Waals forces between single layers because of which they can slide one over another, making it a perfect lubricant. The crystalline or flake form of graphite consists of graphene sheets stacked together.

Graphene is a flat single atom thick planar sheet with densely packed sp^2 hybridized carbon atoms in a honeycomb lattice (Figure 1.1). Graphene is a 2D structure, while there are 0D carbon structures called fullerenes, 1D tubes called carbon nanotubes, and stacked graphene layers that form 3D graphite. Graphene nanoribbons (GNR) are narrow strips cut out of an infinite graphene plane. Graphene nanoribbons can be

divided into two different types depending on the edge symmetry. These are zigzag and armchair nanoribbons.

A method for graphene production had a U.S. patent application in 2002 by Jang and Huang (patent issued in 2006)[3]. In 2004 physicists at University of Manchester and the Institute for Microelectronics Technology, Chernogolovka, Russia, isolated individual graphene planes by using adhesive tape[2]. They stuck a flake of graphite debris onto plastic adhesive tape, folded the sticky side of the tape over the flake and then pulled the tape apart, splitting the flake in two. As the experimentalists repeated the process, the resulting fragments grew thinner. Once they made thin fragments, they meticulously examined the pieces and were astonished to find that some were only one atom thick. Even more unexpectedly, the newly identified bits of graphene turned out to have high crystal quality and to be chemically stable even at room temperature.

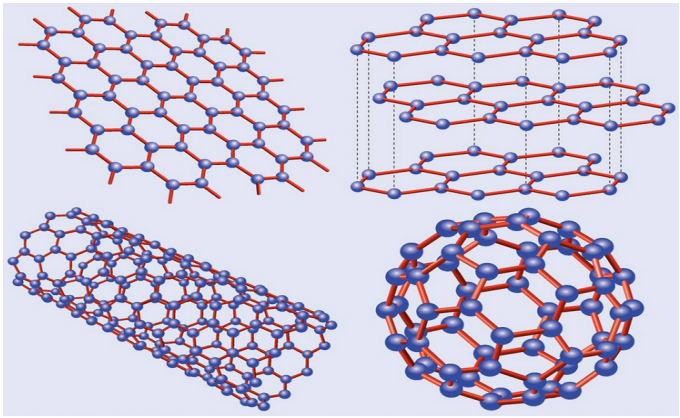

Figure 1.1: Top left two-dimensional graphene (2D), Top right three-dimensional graphite (3D), bottom left one-dimensional nanotube (1D), bottom right zero dimensional fullerene (0D) (Castro Neto et al [4]).

1.1.1 Graphene synthesis and properties of nanoribbons

After graphene invention, the biggest challenge for the researchers is to find ways to synthesize graphene in large scale. Graphene can be synthesized by epitaxial growth on different substrates[3].It is well known that the graphene flakes can be produced by rubbing down graphite on a surface[2]. Another method the researchers came up with for the synthesis of graphene is by unzipping carbon nanotube [4]

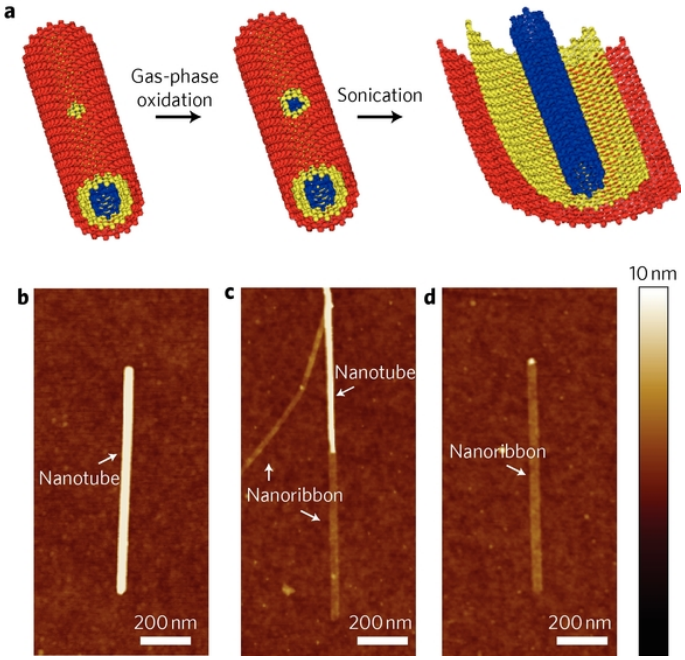

Figure 1.2: AFM image of tube unzipping which proceeds from b-d. (Jiao et al[7])

Another promising technique is exfoliation of graphene from graphite using different surfactants in solution[8].

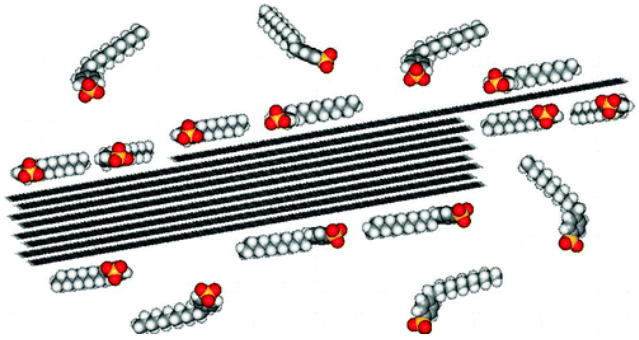

Figure 1.3: Interaction between surfactant molecule and Graphene platelets during exfoliation (Pupysheva et al.) [8]

Graphene has a bond length and bond angle of 1.42 Å and 120° respectively

As for zigzag and armchair graphene nanoribbons, because one can draw two aromatic resonance structures of zigzag and one aromatic structure for armchair ribbons, zigzag ribbons are more conductive than armchair ribbons [9].Both zigzag and armchair ribbons exhibit ferromagnetism when doped, making them magnetic semiconductors, which act as both storage and switching units [9]. Monoatomic layer of graphene has unexpectedly high opacity [10]. Graphene has mechanical strength 200 times greater than that of steel with a tensile modulus of 1TPa [11].

1.2 Electronic Transport in Graphene Nanoribbons and Possible Applications

According to the electronic properties, graphene is considered to be a two-dimensional semi conductor with zero band gap. In GNR change in the width varies the band gap of the structure near the Fermi level. Increase in the width of GNR decreases the band gap. Electronic properties of the GNR depend on the type of nanoribbon. As we have discussed in the Introduction, there are two types of graphene nanoribbons one is zigzag and the other is armchair. Zigzag GNR has dispersion less state at Fermi energy. When electric field is applied across the width of the nanoribbon, zigzag nanoribbon acts as a semi-metallic system[12]. Unlike the zigzag case, armchair nanoribbon band gap does not depend on the edge state, instead metallicity of a given armchair GNR depends on its width[13]. Although metallic graphene nanoribbon exists theoretically, no experimental result has yet supported this conclusion. Even a slight disorder in the nanoribbon will induce a gap.

Companies like IBM and Intel are now welcoming new materials to replace silicon. Ballistic electron transport of graphene nanoribbon at room temperature helps in building micro-electronic structures. Some of the different applications of electronic

transport in the graphene nanoribbon are gas sensing [14,] single-electron graphene transistor [15],spin transistors [16], liquid crystal, and solar batteries [17].

1.3 Defects

During the synthesis process of graphene there may appear some defects in the output. With the recent advances in technology, scientists were able to find techniques to minimize the defects in the output but complete removal of defects is generally not accomplished. Many research works are conducted to understand the reason of defects formation and to understand different properties of graphene with those defects.

Basically there can be point defects and line defects in graphene. Here we discuss different point defects in graphene. Various types of point defects that are observed so far in graphene are as follows

Vacancy Defect

Adatom Defect

Adatom-Vacancy pair Defect

Stone-Wales Defect

Inverse Stone Wales Defect

Octagonal and Pentagonal Defects

Flower Defect

These different defect types will be introduced and studied in details in later sections.

1.3.1 Negative and positive impacts of defects on GNR

Defects that are found in graphene nanoribbons sometimes are found to be very useful in different applications, whereas some defects destroy desired characteristics such as the excellent electrical properties of graphene nanoribbons. In this section we discuss different impacts of defects on graphene nanoribbons and their possible applications.

1.3.1.1 Positive impacts of Defects on GNR

Hydrogen Storage: As many researchers main concentration is to find renewable and clean energy sources, lot of attention has been drawn by graphene due to its unique abilities. It is found that buckled graphene nanoribbons, where some of the carbon atoms become close to sp^3 hybridized, will have convex shaped bumps on their structures. Tozzini et.al [18]found that that the hydrogen molecules, that constitute a

major renewable energy carrier, are attracted more towards buckled graphene than flat graphene.

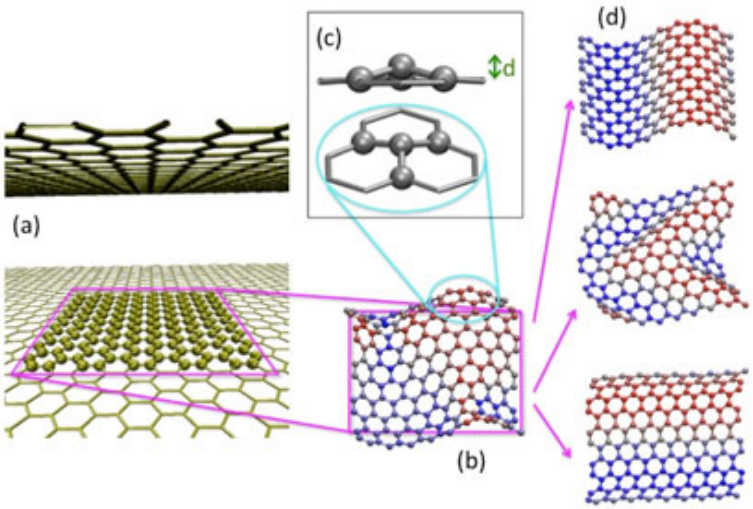

Figure 1.4 (a) Flat Graphene (b) Buckled graphene (c) Inset of Buckled graphene (d) possible buckling's that observed in graphene nanoribbon (Tozzini et.al [18])

Conductance: Pentagonal octagonal pair defect has pentagon and octagon rings inside the graphene nanoribbon in a linear fashion. STM image of the pentagonal octagonal defect is shown in the figure 1.5. It is observed that POP when induced makes the graphene nanoribbon acts a 1D metallic wire. This is considered to be a positive impact on the graphene nanoribbon as it makes the structure as 1D metallic wire.

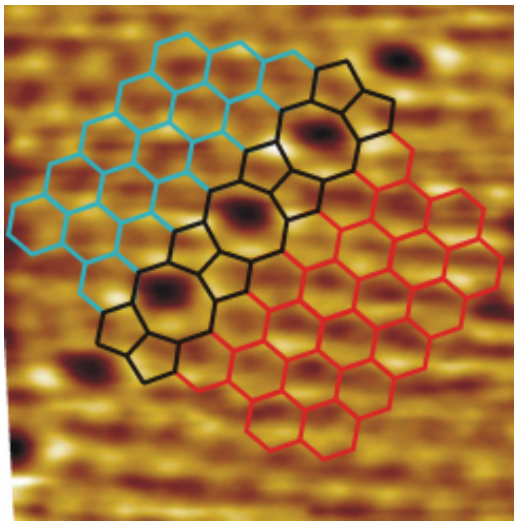

Figure 1.5 Possible locations of Li atom on GNR (Tang et.al [19])

Sensors: Sensitivity of graphene to different molecules and atoms in atmosphere helps in creating different sensors, which detect harmful gases in the atmosphere. When a specific gas is present in the atmosphere, depending on the molecule characteristics, the molecules may get adsorbed on graphene without distorting its hexagonal lattice with possible change in the conduction properties of GNR [20]. Recently researchers found that each gas produces a certain low frequency noise, which can be reproduced [21]. This can help in determining the specific gas present in the atmosphere. Figure 1.6 shows a sample gas sensor based on conductance change of graphene.

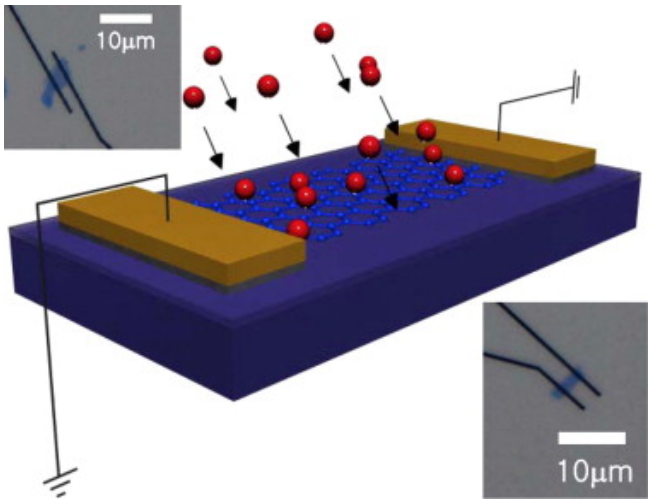

Figure 1.6 Graphene as gas sensor (Geim et.al[22])

1.3.1.2 Negative impacts of defects on GNR

Tensile Strength: Stone-Wales defect is one of the defect types where a C-C bond rotates by 90° creating pentagonal and heptagonal pairs in the structure. As graphene has very good mechanical properties, it is important to understand the impact of defect on the mechanical properties. From the results of Cheng et al.[23],stone wales defect destroys the tensile strain and reduces the strength of GNR. According to the results obtained by Cheng et al., ideal strength of GNR is decreased from 120 GPa to 94 GPa and tensile strain is decreased by 15% when Stone-Wales defect is induced in the graphene nanoribbon. Figure 1.7 shows the pristine and the defected nanoribbons considered.

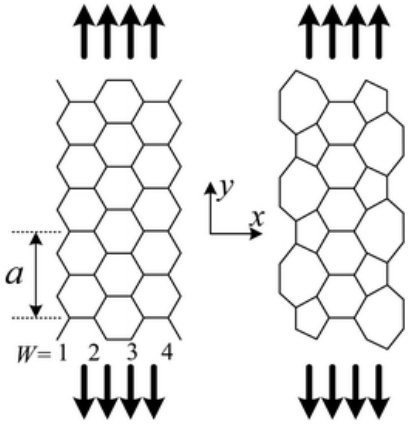

Figure 1.7 Pristine zigzag GNR (left) and defected GNR (right) under tensile stress (Cheng.et al.[23]).

Thermal Transport: With the advancement of new technologies and equipment, many research works have been carried out on new materials to investigate heat dissipation in electronic devices. Phonons in the structure play a vital role in the determining its thermal transport. Zhang et al.[24] have performed simulations on a GNR with vacancy defect to study the impact of defect on thermal transport. According to their results,8.25% vacancy defect decreases the thermal conductivity from 2900 W/mk to 3W/mk.

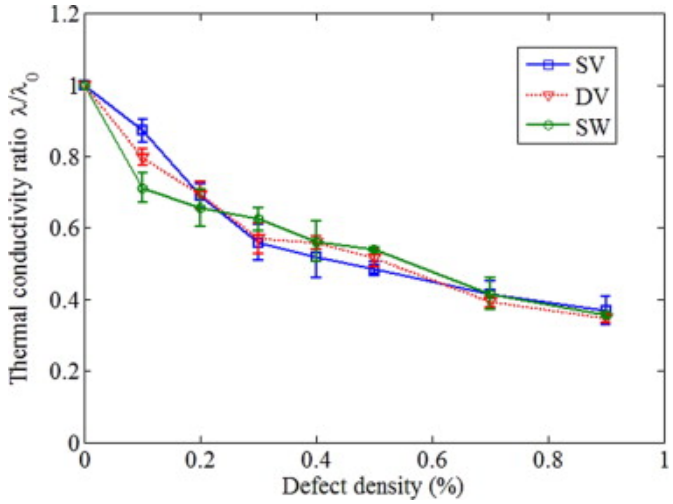

Figure 1.8 Thermal transport (Zhang et al.[24])

Conductance of GNR: Graphene is well known for its unique electrical properties. GNR conduction depends on the type of defect present in the nanoribbon. From the results of Gorjizadeh et.al[25] it has been found that vacancy defect decrease the conductivity of GNR depending on the position of the defect. It has been reported that when the vacancy moves to the edge for zigzag graphene nanoribbon thereis no change in conduction. Different locations considered for a vacancy defect in GNR by Gorjizadeh et.al are shown in the Figure 1.9.

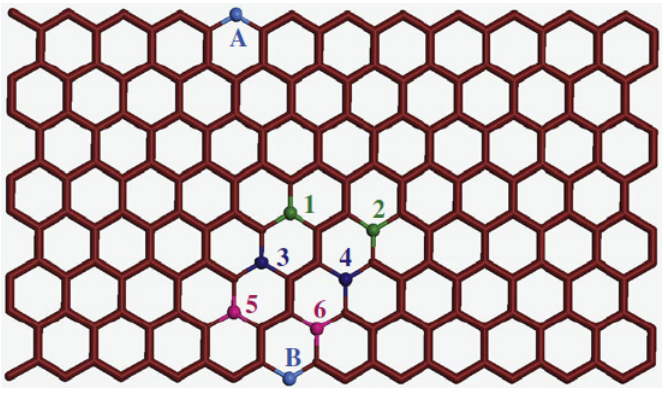

Figure 1.9 Vacancy defect and its possible locations on azigzag graphene nanoribbon of width 8 zigzag chains (Gorjizadeh et.al [25]).

1.3.2Various Defect Types

1.3.2.1 Vacancy Defect

Vacancy is a type of point defect observed in crystals. Vacancy formation is an endothermic process, as vacancy defect in any crystal can be obtained by breaking bonds. This is a kind of defect that occur due to missing or removal of some atoms at their respective lattice site in a graphene nanoribbon. Using Scanning Tunneling microscope one can visualize the vacancy defect in a given nanoribbon. This kind of defect can be formed by electron irradiation on a localized area of the graphene nanoribbon. Vacancy characterization is shown in Figure 1.10.

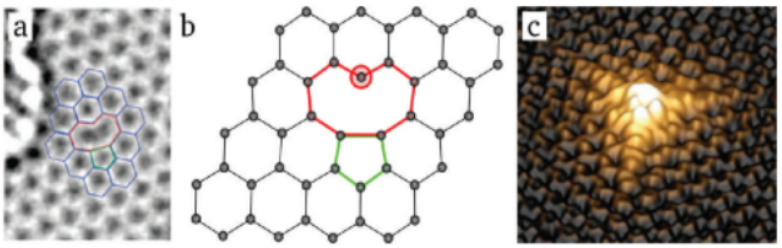

Figure 1.10: Graphene vacancy defect: (a) Experimental TEM results (Meyer et al.[26]) (b) Atomic structure from DFT calculations (Brihuega et al.[27]) (c) Schematic 3D view of (b).

1.3.2.2Adatom Defect

Interstitial atoms are one of the defect types that one may observe in crystals. But, placing an atom in an interstitial position in the graphene lattice needs a high amount of energy. So interstitials defect is not energetically favorable in graphene lattice. Adatom is a type of defect ,which can be created by adding an atom on the graphene nanoribbon. This type of defect is similar to interstitial defect as in both cases we add atoms to the structure (Figure 1.11).

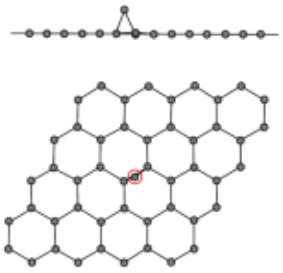

Figure 1.11: Side and top views of a single adatom defect in graphene nanoribbon (Banhart et al.[28]).

1.3.2.3Adatom Vacancy Pair

Combination of both adatom defect and vacancy defect gives rise to a new defect called adatom-vacancy defect. Adding an adatom near vacancy defect in graphene nanoribbon can form this defect. Migration of atoms takes place in this kind of setting and the adatom migrates to the vacancy region and forms this new type of defect. Two adatom-vacancy structures are shown in the Figure 1.12.

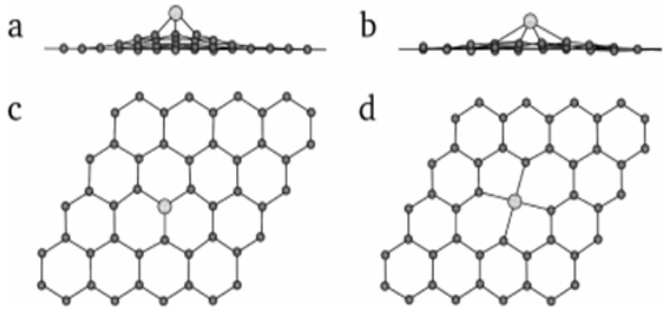

Figure 1.12: (a) and (c) represent side and top views of single-adatom-single-vacancy whereas (b) and (d)represent the side and top views of single-adatom-double-vacancy. Smaller dark circles represent carbon from graphene lattice, whereas the bigger lighter circles represent adatom (Banhartet al [28]).

1.3.2.4Stone-Wales Defect

Stone-Wales defect is formed by 90° rotation of two carbon atoms about the midpoint of a C-C bond. During this process 4 hexagons will convert into 2 pentagons and 2 heptagons. Unlike the adatom defect and vacancy defect, Stone-Wales defect have the same number of carbon atoms in the nanoribbon as the pristine graphene nanoribbon of same width. The mechanism of the bond rotation is shown in Figure 1.13.

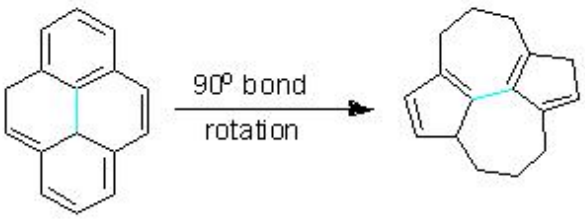

Figure 1.13: Formation of Stone-Wales defect (Mauter et al.[29]).

1.3.2.5Inverse Stone-Wales Defect

This kind of defect is formed by a di-vacancy. This defect is composed of two pentagons and two heptagons. Where two pentagons are arranged adjacent to each other, with a common C-C bond. For comparison, in the Stone-Wales defect heptagons are arranged adjacent to each other, with a common C-C bond. As the arrangement of pentagons and heptagons is inverse to that of the Stone-Wales defect, this defect is called inverse stone wales defect. According to Lusk et al.[30]inverse stone wales defect is an irreversible defect. Inverse Stone wales defect in a graphene nanoribbon is represented in Figure 1.14.

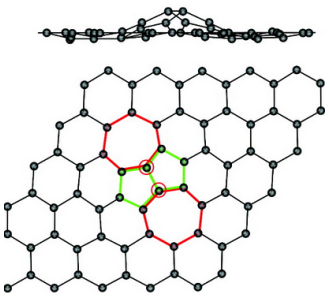

Figure 1.14: Side and top views of inverse stone wales defect (Banhart et al.[28]).

1.3.2.6Octagonal and Pentagonal Defect

Octagonal and pentagonal defect is formed due to the rearrangement of multi vacancies in the graphene nanoribbon. This kind of defect includes two pentagons adjacent to each other and an octagon next to these two pentagons. Bond rotation in

this structure can re-arrange the structure into three pentagons and three heptagons. STM image of octagonal and pentagonal defect in graphene is shown in Figure 1.15.

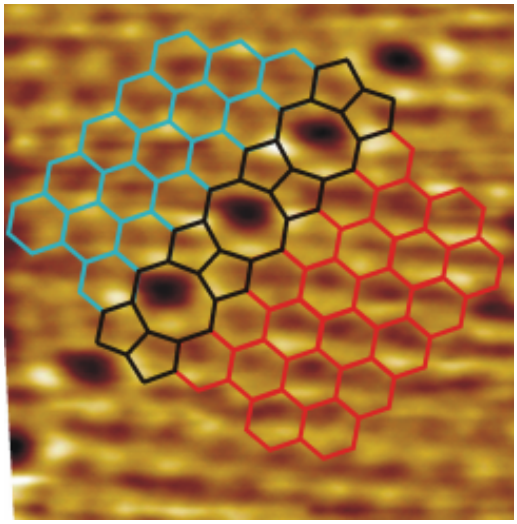

Figure 1.15: STM image of octagonal and pentagonal defect in graphene nanoribbon (Lahiri et.al [31]).

1.3.2.7Flower Defect

Flower defect is a nonlinear topological defect consisting of pentagonal and octagonal circular rings. According to researchers [32], flower defect has lower energy of dislocation compared to Stone-Wales defect, which makes flower defect energetically more favorable. STM image of the smallest member of flower defect is shown in Figure 1.16.When graphene is produced at high temperatures, some of the graphene sections cut loose[32]. When cooled, these sections rotate and patch up on the graphene lattice in a non-linear manner like a flower. Hence this defect is named as flower defect.

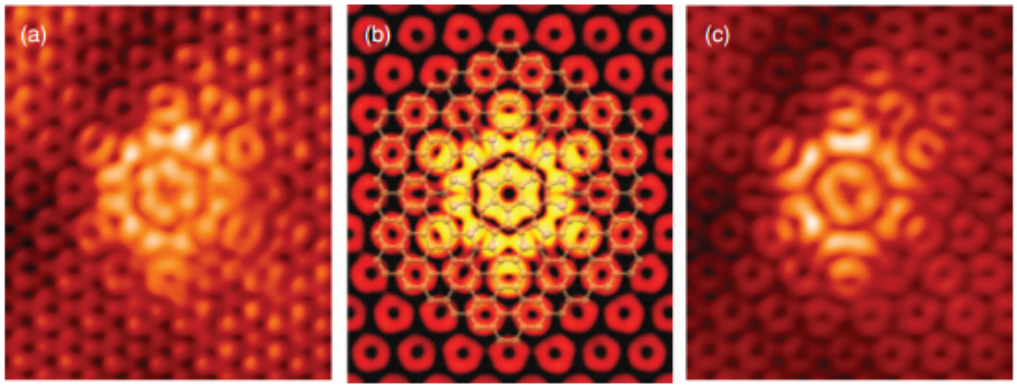

Figure 1.16: STM images of flower defect (Cockayne [32]). (a) and (c) represent experimental STM images whereas (b) represents simulated STM.

1.4 Methods of Defect Characterization

Nanotechnology is not a completely new field, as it was known for a rather long time. It all started with Dr. Richard Feynman, who talked about manipulation of atoms at the atomic level in a classic talk "There is a plenty of room at the bottom" at the annual meeting of American Physical Society held at Caltech 1959. In his talk he presented the concept and the possible issues that we face when electric circuits are prepared in nano level. Characterization tools are among the indispensible necessities of nanotechnology investigations. Here we briefly review various tools that can be used in the study of defects in GNR.

Many equipments are currently used to characterize different nanostructures, including defects. Using SEM, TEM, STM, XRD, SAXS, AFM, SPM, EDX,

XPS/UPS, IR spectroscopy, and Raman Spectroscopy we can characterize nanostructures. In this section I briefly explain mechanisms involved in these methods.

1.4.2 Transmission Electron Microscope (TEM)

Transmission electron microscope can be used in different modes. In imaging mode we can characterize topography, while morphology and composition are characterized in scattering mode. Thermal and mechanical properties are characterized in focused mode. If there is no energy loss, diffraction patterns are observed upon elastic scattering. Energy losses due to grain boundaries, dislocations, defects etc. lead to inelastic interactions inside the apparatus. Schematic representation of TEM is shown in Figure 1.18. One of the experimental example of TEM usage in characterizing graphene has been explained previously for vacancy defect (Meyer et al.[26]).

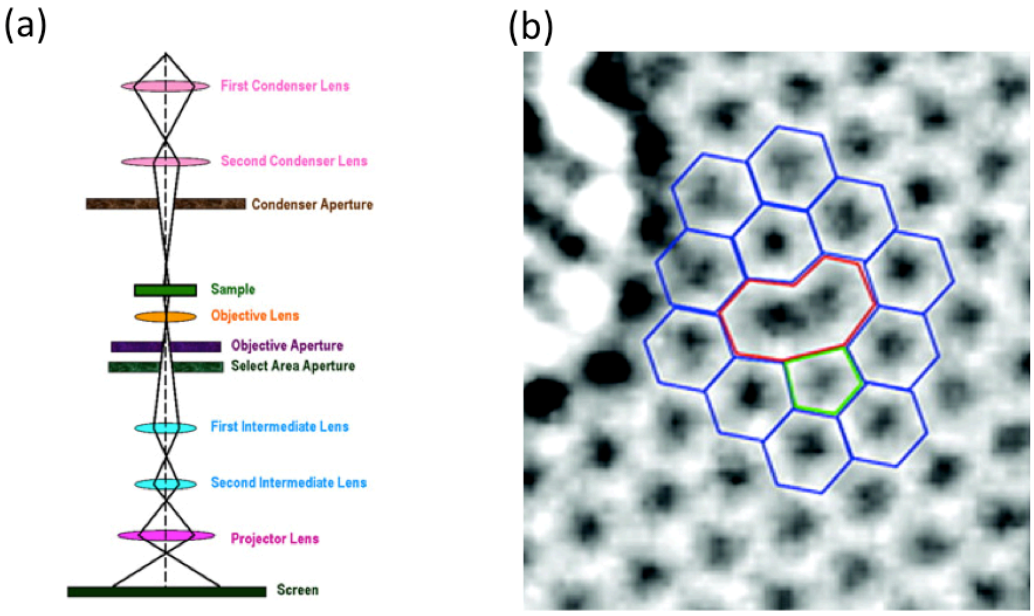

Figure 1.18: Schematics of Transmission Electron Microscope(Mc.Mullan et.al [33]) (a) and TEM image of reconstructed vacancy in graphene (Meyer et al.[26]) (b).

1.4.3 Scanning Tunneling Microscope (STM)

Quantum mechanical tunneling principle is used in STM. STM shows a three dimensional image. A probe is used in the STM to study the structure of the surface. The distance between the probe and the surface is the main key that helps in determining the representation of surface. First the probe is place at a few angstroms distance from the surface of the material and few volts of voltage is applied and the probe is moved along the surface. While moving along the surface, when probe comes close the surface a sharp increase in the tunneling current is observed and vice versa. The tunneling current responses over the surface are converted into a 3D representation that determines the surface characteristics. STM is schematically

shown in Figure 1.19. One of the experimental example of STM usage in characterizing graphene has been explained previously for pentagonal octagonal defect (Lahiri et al[31]).

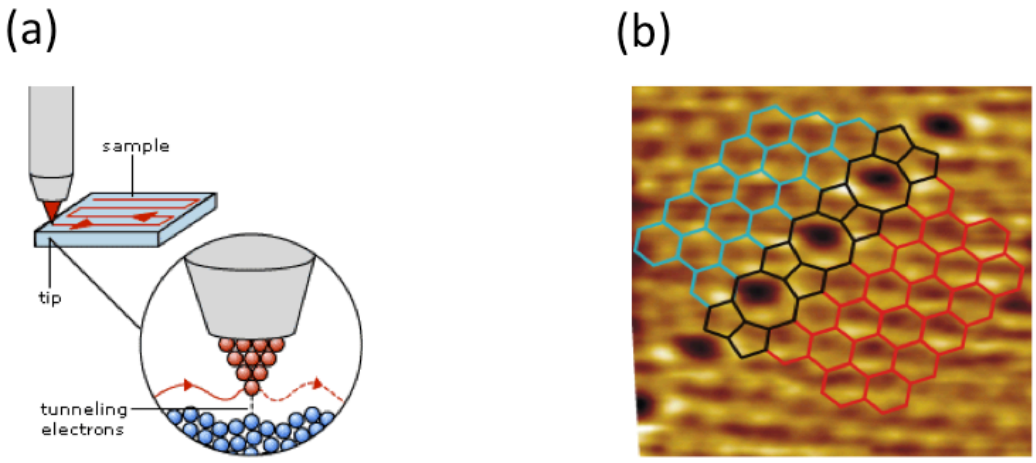

Figure 1.19 Scanning Tunneling Microscope (Crewe et.al [34]) (a) and STM image of pentagonal-octagonal defect in graphene (Lahiri et al.[31]).(b).

1.4.4 X-Ray Diffraction (XRD):

X-Ray Diffraction is used to characterize many aspects of a given specimen like lattice constant, interplane spacing, crystallinity, thickness of film, and the size of the grains. Principle of XRD functionality is based on Bragg's law. In XRD a monochromatic X-ray is projected on the specimen surface at an angle of θ. By using Bragg's law diffraction at each angle of incident is determined. After determining all the values, a graph based on the angle between diffraction and the incident beams is plotted which will help in investigating different properties of the specimen. A

schematic diagram of X-ray diffraction is depicted in Figure 1.20. XRD characterization of graphene thin films that are synthesized by chemical reduction of exfoliated or intercalated graphene oxide has been done by Thema et al.[35].

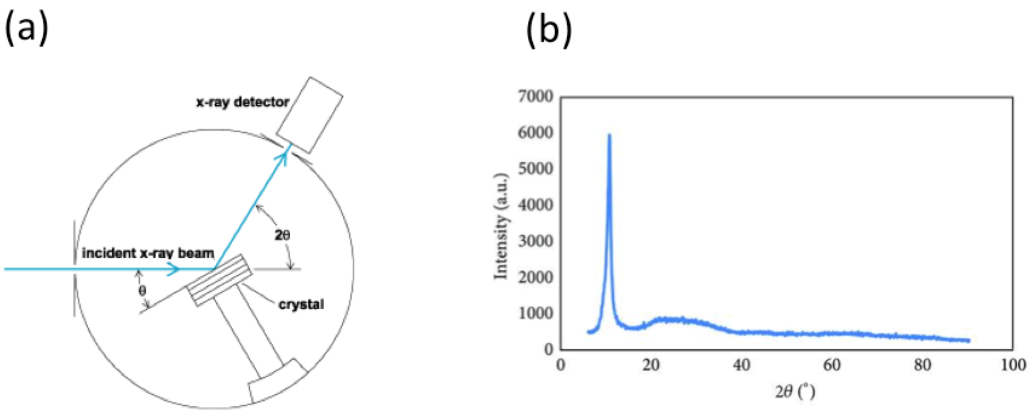

Figure 1.20: Schematic diagram of X-ray diffraction (Greenouoh et.al [36]) (a) and XRD diffractogram of graphene oxide (Thema et al.[35]) (b).

1.4.6 Atomic Force Microscope (AFM)

Atomic Force Microscope (AFM) is also called Scanning Force Microscopy. AFM is used to scan the specimen surface. In AFM there is a cantilever beam with a sharp probe, when the probe comes close to the surface and when it touches the surface then there will be a deflection in cantilever. Basically the force between specimen and the cantilever tip is maintained constant. But when the probe (tip) in AFM comes close to the surface, surface electrons of the specimen repels the electrons on the tip and this

changes the force between surface and specimen. To restore the force the probe adjust itself which creates deflection in the cantilever beam. This movement of the probe while moving along the surface is tracked and creates a 3D image of the sample. Laser is used to detect and track the movement of the cantilever tip and the specimen is placed on a piezoelectric material, which helps in determining the variation in current. AFM apparatus is schematically shown in Figure 1.22. One of the experimental example of AFM usage in characterizing graphene has been explained previously for tube unzipping (Jiao et al[7].).

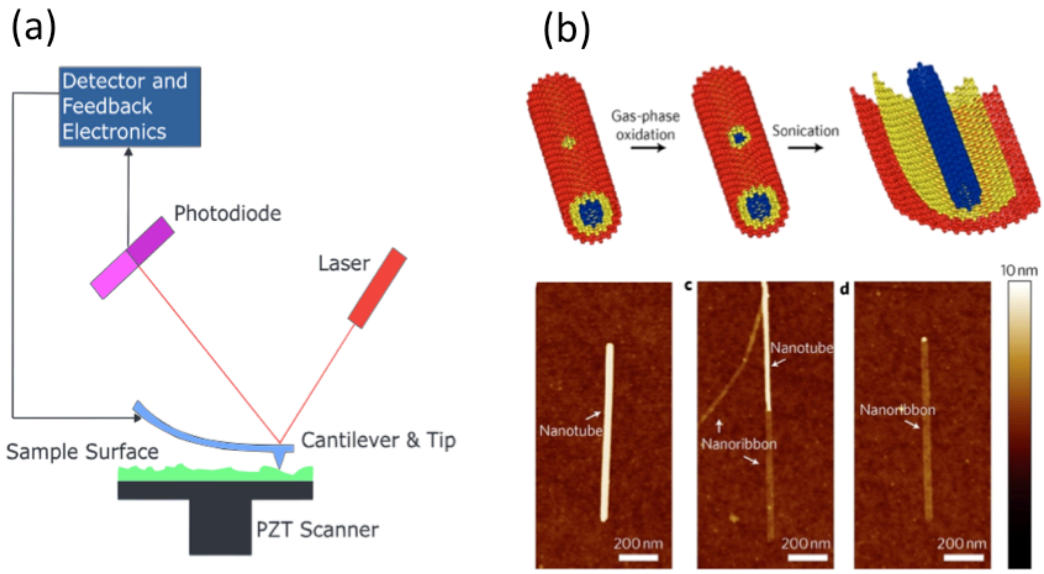

Figure 1.22: Atomic Force Microscopy (Lang et al [37]) (a) and AFM images of pristine, partially and fully unzipped nanotubes (Jiao et al.[7]) (b).

1.4.7 Scanning Probe Microscope (SPM):

Scanning Probe Microscopy is a more general version of STM and is used to characterize topography, magnetic, thermal, electrical, mechanical and chemical properties of a given specimen. In this microscopy, probe is moved across the surface that scans the whole surface and helps in determine the properties of given specimen. Different properties of the specimen are determined by using different probes of the SPM. Depending on the type of the interaction between probe and the specimen there are so many types of SPM like Scanning Tunneling Microscopy, Magnetic Force Microscopy, Magnetic Resonance Microscopy, Scanning Capacitance Microscopy, Force Distance Microscopy, Elastic Modulus Microscopy etc. Main principle of SPM is shown in figure 1.23. One of the examples of characterizing graphene using SPM technique was performed by Nagase et al [12] to characterize epitaxial graphene domains on partially graphitized SiC.

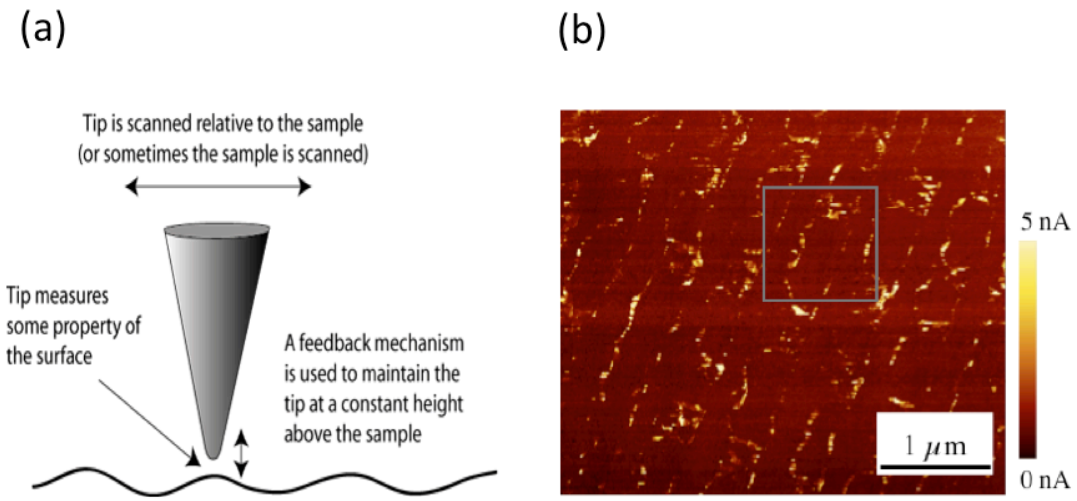

Figure 1.23: Scanning Probe Microscopy (Goldstein et al.[37]) (a) and characterization of epitaxial graphene domains (Nagase et al [12]) (b).

1.4.9 Photoluminescence (XPS, UPS)

Photoluminescence technique is used to characterize composition and concentration of different elements present in the given specimen. Emission of light in this process can be due to a variety of stimulations. For example, if there is an electron stimulation then the photoluminescence is called as cathodoluminescence. When X-rays are used to excite the electronsfrom a lower energy state to a higher energy state of the given sample, then it is called X-ray photoelectron spectroscopy(XPS). Likewise if Ultraviolet rays are used to excite the electrons in the given specimen then it is called ultraviolet photoelectron spectroscopy (UPS). XPS is used to examine core levels whereas UPS is used to examine valence levels of the specimen. XPS and UPS methods are schematically represented in Figure 1.25. Characterization of reduced graphene nanosheets are performed using XPS by Meng et al [38].

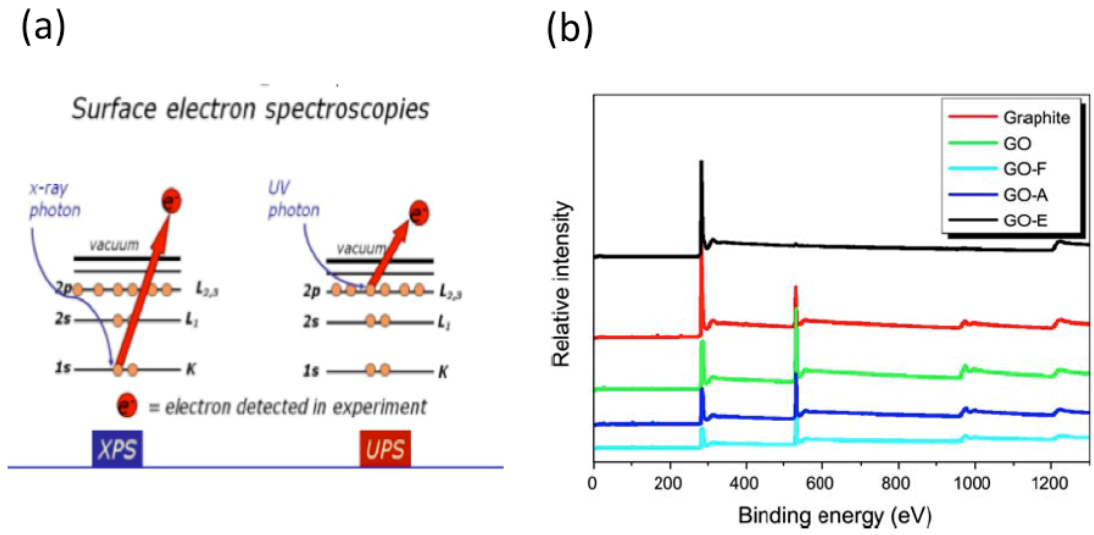

Figure 1.25 XPS and UPS (Turner et al.[39]) (a) and XPS spectra of graphite flakes and graphite oxide sheets before and after the different pre-treatments (Meng et al. [38]) (b).

1.4.10 Infrared Spectroscopy

Infrared (IR) Spectroscopy is used to characterize composition, concentration and atomic structure of different elements in a given specimen. Molecules and crystals in the specimen are compared to the famous spring-mass system where atoms or ions are considered as the mass and the chemical bonds between atoms are considered as spring. When the IR frequency matches with the vibrational frequency of atoms in the system, absorption of energy occurs. Examining the absorbed IR frequencies helps in understanding the vibrational modes present at a given frequency. Analysis of the IR spectrum provides different aspects of molecular structure of the sample. Sample IR spectrum is provided in the Figure 1.26. One of the experimental example of Infrared

spectroscopy usage in characterizing bilayer graphene is reported by (Kuzmenko et al[40]).

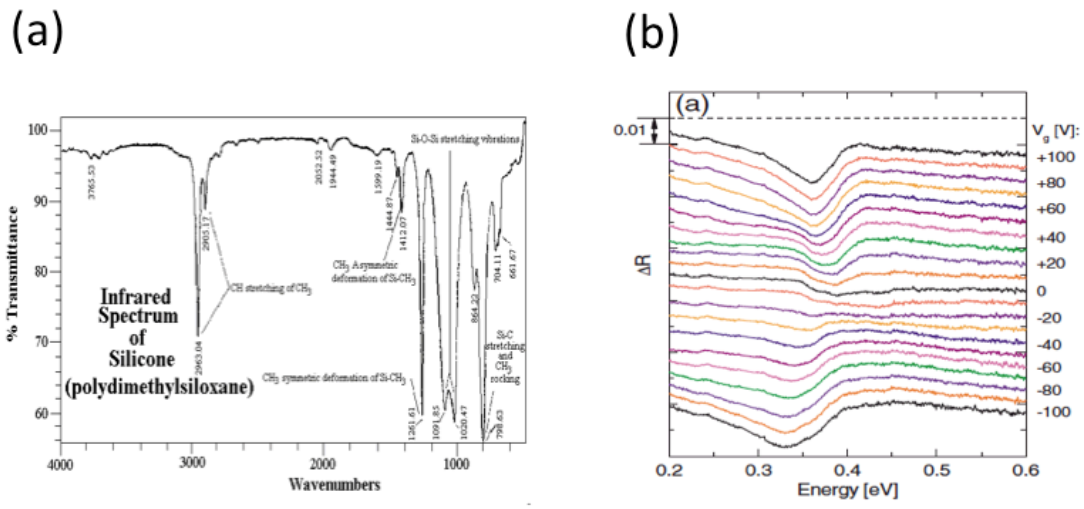

Figure 1.26: IR spectrum of silicone (Lau[41]) (a) and IR spectra of bilayer graphene as a function of gate bias (Kuzmenko et al.[40]) (b).

1.4.11 Raman Spectroscopy

Like IR spectrum, Raman spectrum is used to characterize composition, concentration and atomic structure of a given specimen. Unlike IR spectrum, incident light in Raman spectrum is visible light. When visible light is incident on the surface, photons interact with the electrons in the system and excite them to higher energy states. During de-excitation part of energy is radiated in the form of light. Most of the radiated energy has the same frequency as the frequency of the incident light; this scattering is called as Rayleigh scattering. Excitation and de-excitation of vibrational states may occur by radiation at a frequency different from that of the incident light

via Stokes and anti-Stokes mechanisms. Raman spectroscopy mechanism is schematically shown in Figure 1.27. Different graphene patches produced by exfoliation technique are characterized by Malard et.al [42] using Raman spectroscopy.

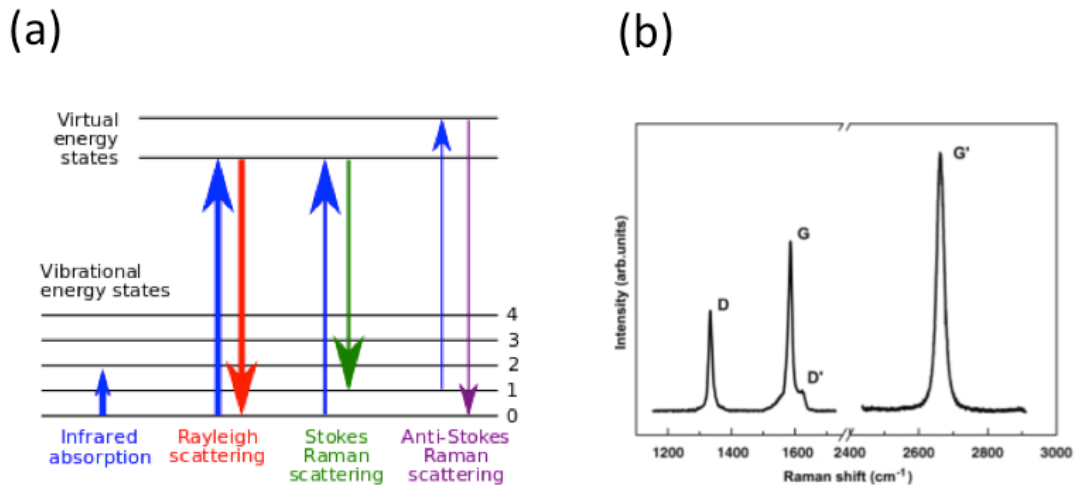

Figure 1.27: Raman Spectroscopy (Gardiner[43]) (a) and Raman spectrum of a graphene edge (Malard et al. [42]) (b).

2. Method

2.1 Computational Materials Methods

The quantum theory addresses atomic and molecular level physical phenomena. It is in principle possible to apply quantum theory to complex systems, which have many number of atoms. To achieve this aim, however, several levels of approximations are necessary. Computational materials science makes use of the advanced computational hardware/software to solve basic quantum mechanical equations, with proper simplifications and approximations, for realistic materials.

Nearly all-physical properties depend on the energy or the difference between total energies of systems. Every system tends to minimize its total energy to attain equilibrium; even the defects in the system tend to attain the minimum total energy value. So, it is very likely that by calculating the total energy of the system we can compute its different physical properties [44]. For example, to predict the equilibrium lattice constant, we have to find the total energy of the system for different lattice

constants, and by finding the energy minimum we can find the equilibrium lattice constant.

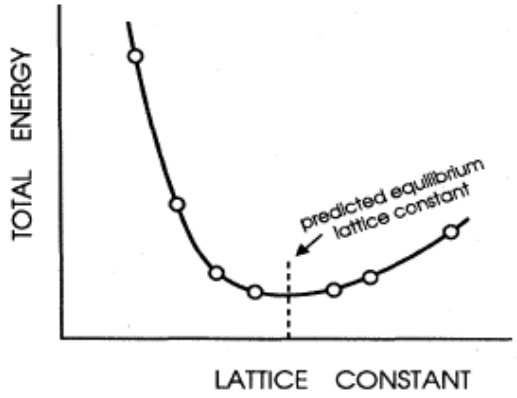

Figure 2.1: Equilibrium lattice constant(Payne et al [44])

Solving the Schrödinger equation is the main step in quantum mechanical description of the system. This allows one to calculate energies, polarizabilites, lattice constants, etc.

Schrödinger equation in it simplest form applies to single particle systems:

$$\hat{H}\psi = E\psi \quad (2.1)$$

where $\hat{H}$ represents Hamiltonian operator, ψ represents wave function and E represents energy of the system.

2.1.1 Hartree-Fock approximation and Density Functional Theory (DFT)

The wave function of a many-electron system should be antisymmetric with respect to the exchange of any two electrons, because electrons are fermions. This property

causes the energy of the system to reduce due to the presence of a term called exchange energy. The approximation that includes such a term is called Hartree-Fock approximation. Other contributions to electron-electron interaction energy beyond exchange interaction are called correlation energy.

For a system containing many electrons and ions, as is the case for any real material, Kohn and Sham showed that the problem can be reduced to a set of simplified single particle problems. The total energy in this scheme is written as[44]

$$E[\{\psi_i\}] = 2\sum_i \int \psi_i \left[-\frac{\hbar^2}{2m}\right] \nabla^2 \psi_i \mathrm{d}^3 r + \int V_{ion}(r) n(r) \mathrm{d}^3 (2.2)$$
$$+ \frac{e^2}{2} \int \frac{n(r) n(r') \mathrm{d}^3 r \mathrm{d}^3 r'}{|r - r'|} + E_{XC}[n(r)] + E_{ion}(\{R_I\})$$

where the terms on the right hand side respectively represent kinetic energy, ion-electron Coulomb interaction, electron-electron Coulomb interaction, electron-electron exchange-correlation interaction, and ion-ion Coulomb interaction. $n(r)$ is the electron density that is equal to $2\sum_i |\psi_i(r)|^2$. The minimum value of E represents the ground state energy of the physical system. The many-body problem therefore can be formulated in terms of the electron density, as the energy functional is a functional of the electron density. Such an approach is called Density Functional Theory (DFT). It

is important to note that various further approximations are necessary to find a reasonable exchange-correlation functional.

Ab initio approaches such as Hartree-Fock, as well as other methods such as DFT, are used in physics and chemistry to investigate the electronic structure (principally that of the ground state) of many-body systems, in particular atoms, molecules, and the condensed phases.

2.1.2Born-Oppenheimer approximation (BOA)

According to this approximation, electrons move faster than nuclei in the atoms. In this case one supposes that nuclei have no kinetic energy. BOA therefore divides wave function of the system into electronic and nuclear components. The Hamiltonian with no movement of nuclei is considered to have $3n$ coordinates of electrons. Therefore the Hamiltonian now depends on the position where the nuclei are sitting as electron nuclear attraction and nuclei-nuclei repulsion vary regarding the positions of nuclei. This new Schrödinger equation is called electronic Schrödinger equation

$$H^{O}\Psi_{K}(r \mid R) = E_{K}(R)\Psi_{K}(r \mid R) \qquad (2.3)$$

Here H^0 is Hamiltonian operator in electronic coordinates, its eigen functions form a complete and orthogonal set of functions of r and ψ_K represents Eigen function of H^0.

Relation between $\psi$and ψ_K can be written as a summation of electronic wave functionswith its coefficients as,

$$\Psi(r,R) = \Sigma_K \Psi_K(r,R)\aleph_K(R) \qquad (2.4)$$

Here, χ_k represents vibrational, rotational wave functions of the electronic state. Comparing Equation (2.3) with full Schrödinger equation ($H\psi=E\psi$) where the H includes the Hamiltonian operator (H^0) and kinetic energy of nuclei, we see that Equation (2.3) is a Schrödinger equation that has a potential energy that depends on inter-nuclear positions.

The BOA gives rise to the concept of surface energy potential which in turn gives rise to vibration and rotational electronic wavefunctions. One cannot neglect non-adiabatic terms, if one has two electronic states whose potential surface terms depend on electrons. These non-adiabatic couplings can induce transitions among the states.

2.2 Coherent Transport and Green's function formalism

Electronic transport through various nanostructures can be calculated under the assumption that no inelastic electron scattering occurs. Such a coherent approximation is generally reasonable at low temperature, where lattice vibrations are minimal.

The main assumption in the coherent Green's function formalism is that the device is so small that electrons move from one contact to another with no loss in energy, as the finite nanodevice is placed between semi-infinite length of left and right contacts which does not interact with the nanodevice. The Hamiltonian of the entire device can be written as [45]

$$H = \begin{pmatrix} H_L & -\tau_L & 0 \\ -\tau_L^+ & H_0 & -\tau_R^+ \\ 0 & -\tau_R & H_R \end{pmatrix} \qquad (2.5)$$

Where H_o represents the device Hamiltonian that is at the center part, H_L and H_R represents Hamiltonians of left and right contacts, τ_L and τ_R represents couplings of left and right contacts with the center part, respectively. The Green's function matrix can be determined by using the following equation

$$\left(EI - H\right)G(E) = 1 \qquad (2.6)$$

Where E represents energy of conducting electrons, H represents Hamiltonian, I represent identity matrix and G represents Green's function. There are two types of Green's functions; advanced and retarded, which physically represent incoming and outgoing waves that are formed through excitation. Advanced Green's function is the Hermitian conjugate of retarded Green's function. According to Landauer [46] conductance C can be calculated using formula.

$$C = 2e^2T / h \quad (2.7)$$

Where T is the transmission function, e is the charge of the electron and h is Planck's constant. Transmission function can be calculated using formula [47]

$$T = T_r\left[\Gamma_L G^r \Gamma_R G^a\right] (2.8)$$

Where T_r represents trace operator, i.e. it takes the trace of the matrix on which it acts, $\Gamma_L$and $\Gamma_R$represents coupling factors of left and right contacts and G^r, G^a represent retarded and advanced Green's functions. The total Greens function can be represented as [48]

$$G = \left(EI - H - \Sigma_L - \Sigma_R\right) \qquad (2.9)$$

where H represents Hamiltonian of the conduction part of the system that is sandwiched between the left and right contacts, and $\sum^r$and $\sum^a$ represent retarded and advanced self-energies[48,49]. This concept can be extended to other type of interactions that can occur in the system like electron-phonon interactions.

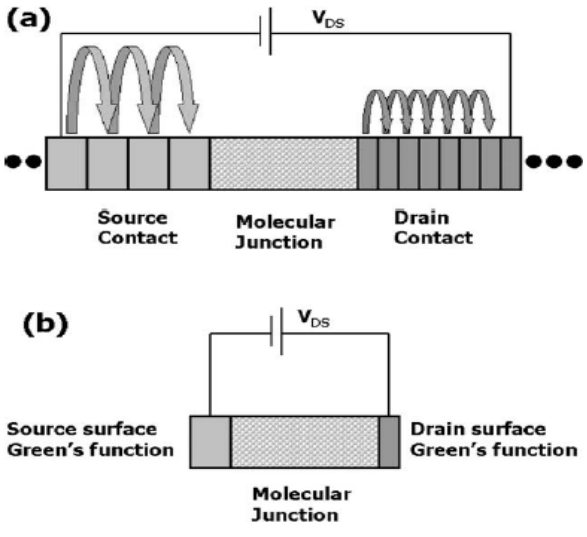

Figure 2.2 : (a) Propagation of excitation from source to drain, (b) modeled surface Green's function for (a) (Farajian et al.[49]).

For doing research on the defected structures we have employed the Green's function formalism for calculating the coherent transport, by using TARABORD program [49,50] which is based on non-equilibrium Green's function approach. The assumptions of TARABORD program are shown Figure 13. Source in the diagram indicates the left contact, molecular junction represents the center conducting part, and drain represents the right contact. Left and right contacts are divided into principal layers, which are assumed to interact only with their nearest neighbors. Molecular junction part is assumed to have the interaction with the surface principal layers of both left and right contacts. To calculate conductance using TARABORD, first we obtain overlap (*S*) and Hamiltonian (*H*) matrices from electronic structure calculations. These are taken as inputs for TARABORD calculations.

After obtaining Hamiltonian and overlap matrices of the system we calculate the surface Green's functions of the left and right contacts. The total Green's function is next calculated by projecting onto the center junction region. TARABORD program uses a powerful algorithm [51] for calculating the surface Green's functions. The resulting transmission function is used to calculate the propagation of excitation from

left contact to central junction and from central junction to right contact. This is accomplished by matching the surface Green's functions of left and right contacts with central junction.

It should be mentioned that we consider ballistic transport for calculating conductance, where each band contributes two (for two spin orientations) quantum units of conductance $(2e^2)/h$. The conductance thus obtained is based on Landauer's [52] interpretation, and belongs to the whole (infinite) nanoribbon with or without defect, not per unit lenght.

2.3 Computational Details:

In this research for electronic structure computations and structure relaxations we have used Gaussian 09 program[53]. These are the two main steps for modeling the defected graphene nanoribbons in our research.

Relaxation: This type of process is used in bringing structures to equilibrium. In this process the atoms are displaced with a small magnitude from their original position and energies at different positions are computed. A given structure is said to be relaxed at the position where the total energy is minimum. Different methods in

Gaussian software to relax the structure include Hartree-Fock (HF) approach and methods based on density functional theory (DFT).

Energy: Energy calculations in this thesis work have been performed using DFT based on BLYP functional. BLYP usesthe exchange functional of Becke and the correlation functional of Lee, Yang and Parr. Liu et.al [54] have concluded that for systems with covalent bonds BLYP calculation results are more accurate compared to some other DFT calculations including local density and generalized gradient approximations (LDA and GGA, respectively). B3LYP, an improved version of BLYP, is also used in our simulations.

Frequency: After structure relaxation, we have performed frequency calculations using Gaussian to determine vibrational frequencies of different structures. It turns out that HF gives poor frequency values [55].

Infrared Spectrum: According to infrared spectroscopy, the atoms in the given structure absorb the vibration frequencies that are characteristic to their structures. Atoms in the structure resonate with the absorbed radiation. For a system of N atoms, if a given structure is linear then it has $3N$-5 vibrational modes. For non-linear

structures there are 3*N*-6 vibrational modes. If a given vibrational mode is associated with a change in the molecular dipole moment, then the mode is said to be IR active. Out of different methods implemented in Gaussian program, MP2 is the best method to compute IR activities [55].

Raman Spectrum: Raman spectrum is used to study vibrational, rational and other low frequency modes of the given system [56]. Laser light interacts with the molecular vibrations and phonons in the given system causing the excitation in the sample. The shift in the energies of the scattered photons provides information of the phonon vibrational modes. Within Gaussian program, B3LYP provides best Raman results [55]. Intensity of Raman band is given as follows[55]

$$I_k = \frac{N(v_0 - v_k)^4 S_k Q_k^2 P}{\left[1 - \exp\left(\frac{-hcv_k}{kT}\right)\right]} \qquad (2.9)$$

where$N$is a proportionality constant, $v_0$is the exciting laser wavenumber, $v_k$is the wave number of the vibrational mode,cis the speed of light,$h$and$k$are Planck's and Boltzmann's constants,$T$is the temperature,$P$is the exciting laser irradiance, and$Q_k^2$is an amplitude factor, S_k represents Raman activity.

Basis Set: A basis set is used to convert Schrödinger equation into a matrix equation. Within the GAUSSIAN program, atomic orbitals basis functions are expressed in terms of Gaussian functions. In our calculations, basis sets 3-21g and 6-31g are used. The basis set 3-21g, e.g., means that three Gaussian functions are summed for core atomic orbital basis functions, while valence orbital basis functions contain two functions each, with the first being expressed as the sum of two Gaussians and the second as a single Gaussian function.

3.Results and Discussion

In this chapter we discuss our results on defected graphene flakes and nanoribbons. Various characteristics of defected graphene including stability, vibrational properties, and transport are considered.

3.1 Stability of Defects:

Vibrational spectra are calculated for the structures whose first partial derivatives of energy with respect to atomic displacement/ coordinates equal zero. Hessian matrix contains the second partial derivative of energy with respect to internal coordinates. From calculus point of view if all second derivatives are positive the curve will be at minimum. A transition state in the given structure is characterized by having single saddle point in the potential energy. Any negative frequency values in the vibrational analysis indicates a transition state which is not a minimum energy configuration and therefore cannot be considered stable.

An understanding of stability of the defects that we are dealing with is necessary before considering their effects on the properties of graphene nanoribbons. In this section we discuss the stability of GNRs with different defects. In this study stability was determined from the results obtained through ab initio and DFT simulations), as discussed in Chapter 2, of small graphene patches (graphene nanoflakes).The results

were also compared with some available experimental results. First we optimizedthe structures and then submitted frequency calculations on each optimized structure using B3LYP method and basis set 6-31G within the Gaussian program. In general a nonlinear molecule with N atoms has $3N$-6 normal modes of vibrations. Gaussian program calculates all the vibrational modes of atoms in the given structure. An example of these vibrational modes is shown in the Figure 3.1. The arrows in the image show the displacement vectors of the vibrating atoms in the given structure.

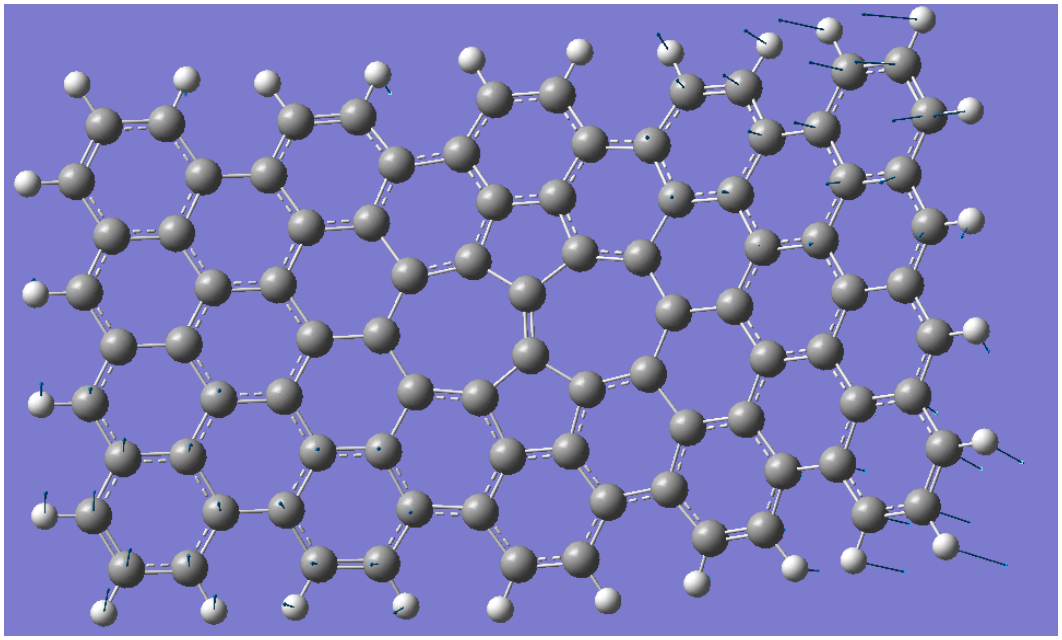

Figure 3.1 Displacement vectors of a typical vibrational mode.

3.1.1 Unstable Structures.

3.1.1.1 Vacancy Defect

Vacancy defect is experimentally observed in graphene by Ijima et al. Ijima et al.[57] induced the vacancy defect using electron irradiation method.Investigations made by the scanning probe microscopy confirmed the presence of vacancy defect. However, HR-TEM image results suggest that vacancy defect is indeed present in nature but are stable for few seconds and disappear[57]. We simulated mono-vacancy defect in graphene using GAUSSIAN programas is shown in Figure 3.1.From Figure 3.1 no significant change is observed upon structure relaxation. However, frequency calculations (to be presented shortly) indicate presence of negative frequencies and we can conclude that the observed vacancy defect is a transition state and not a stable one. This aids the explanation given by the Ijima et al.[57] Hence we conclude that the vacancy defect is unstable in nature.

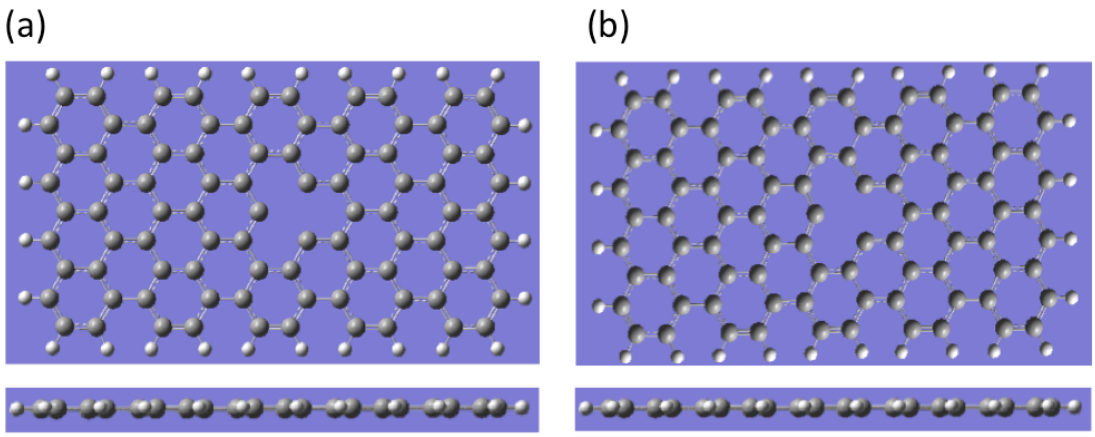

Figure 3.1Structure of a graphene nanoflake with vacancy defect before (a), and after (b) optimization.

3.1.1.2Adatom Defect

Adatom defect is observed experimentally on grapheme layer. According to the experimental studies of Ijima[57], adatom on graphene is stable for a few seconds. Later the adatom moves around and disappear[57]. We simulated the graphene patch with single carbon adatom using GAUSSIAN and results are shown in Figure 3.2.It is seen that to saturate the carbon adatom, two hydrogen atoms are also included. The optimized structure is bent and, as will be shown shortly, we observed negative frequencies, which mean that the adatom defect structure is unstable. In our case we have considered carbon for adatom calculations, but there are cases where elements other than carbon can be used as adatom.

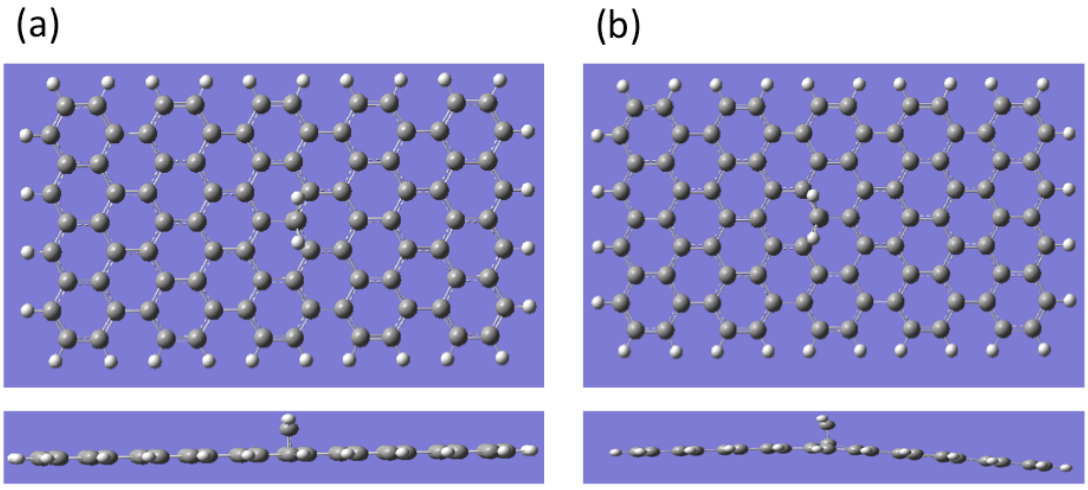

Figure 3.2:Structure of a graphene nanoflake with adatom defect before (a), and after (b) optimization.

3.1.2 Stable Structures

3.1.2.1 Adatom-Vacancy Defect

According to Ijima et al results, adatom-vacancy defect is metastable [57]. Weperformed simulations for this defect using method/bsis B3LYP/6-31g. Before andafter optimization structures are represented in Figure 3.3. We have observed a severely distortedstructure with two heptagons and two pentagons. According toLusk [58],when we place an adatom near a divacancy it will rearrange itself and forms a defect called inverse Stone-Wales defect which we discuss afterdiscussing Stone-Wales defect. It should be mentioned that the stability of adatom-vacancy defect depends on the relative locations of adatom and vacancy. The structure shown in Figure 3.3 is stable owing to the specific relative orientation of the two defects.

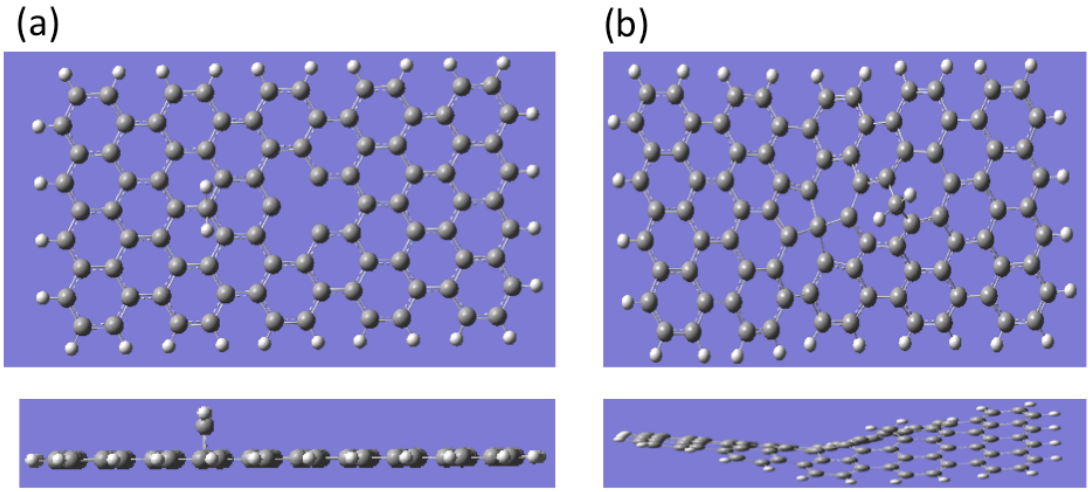

Figure 3.3: Structure of a graphene nanoflake with stable adatom-vacancy defect before (a), and after (b) optimization.

3.1.2.2 Stone-Wales Defect

According to Ijima et al.[57], Stone-Wales defect is a reasonable defect according to stability point of view. Stone-Wales defect (SWD) is energetically stable. SWD is therefore extensively studied. We simulated the SWD on graphene nanoflake and performed optimization. Figure 3.4 shows the top view and front view of graphene layer with SWD before and after optimization. Bending is clearly induced upon optimization, which is in agreement with the experimental observation.

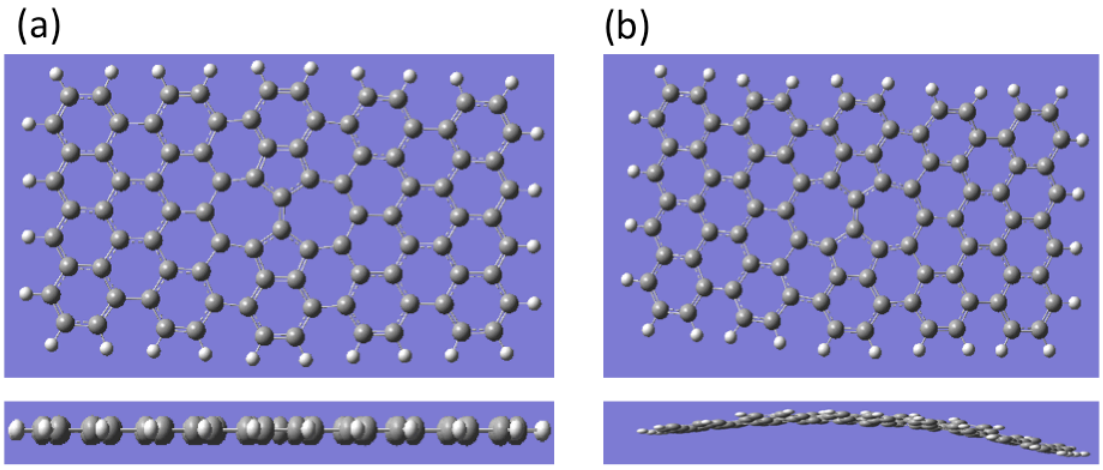

Figure 3.4:Stone-Wales defect before (a) and after (b) optimization.

We see the deformation in the structure after optimization by B3LYP method with basis set 3-21G. Even after submitting the deformed structure for optimization using basis set 6-31G the deformation of the structure still persists. Meyer et al. [26]studies mention the observation of curvature and deformation in the carbon nanotube with SWD. Wang et al.[59] report that curved graphene sheet with SWD is energetically more stable than flat graphene sheet with SWD.HR-TEM images of SWD on graphene by Ijima et al.[57] confirm the presence of bending or distortion of graphene structure during the formation of SWD.

3.1.2.3 Inverse Stone-Wales Defect

Inverse Stone-Wales Defect (ISWD) is a type of defect where pentagons are arranged adjacent to each other. ISWD is not observed experimentally so for but several hints

about their existence is given in the literature[45]. We have created a structure incorporating ISWD in the graphene nanoflake and performed optimization and frequency calculations using B3LYP method with basis set 3-21G. We further validated the results using 6-31g basis. We observed severe bending in the structure. The results are shown in Figure 3.5. The structure, however, is stable according to the frequency calculation results (to be presented shortly).

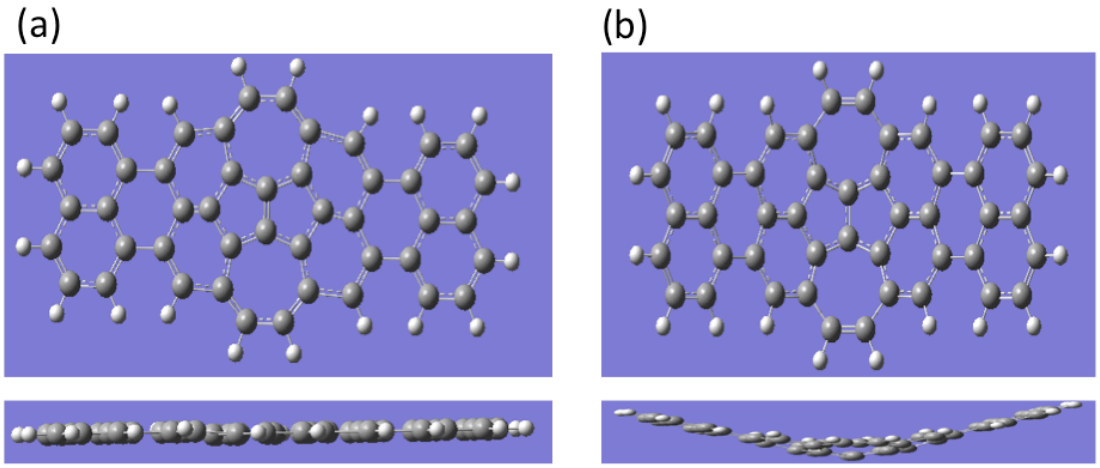

Figure 3.5 Inverse Stone-Wales defect before (a) and after (b)optimization.

Aprevious theoretical work[60]somehow supports our results, as the authors mention that bending is observed in the geometry of graphene having two pentagons adjacent to each other, or when the neighboring cells of pentagon and heptagon are hexagons. Figure 3.6 shows results obtained through DFT calculations[30].It is suggested thatlinear arrangement of ISWD can be helpful in the charge transfer in graphene

electronic appliances[30]. Non-Linear arrangement of ISWD in graphene will produce swelling in the graphene nanostructure as shown in Figure 3.6.

Figure 3.1.6 Nonlinear (a) and linear (b) arrangement of ISWD [30].

Eventhough this defect is not confirmed experimentally our results suggest that ISWD is stable and there are no negative frequencies involved. We can observe deformation in the optimized structure in Figure 3.5, and the deformation is similar to the theoretical result[60].

3.1.2.4 Pentagonal and Octagonal Pair Defect

This defect is observed experimentally[31] and when incorporated in graphene acts as a 1D metallic wire from conduction point of view[31]. The octagons in this defect can promote the selective diffusion of some atoms through the graphene structure. The defect also possess good conductive properties which could bring unique results for nanoelectronics applications. We have optimized the pentagonal-octagonal pair (POP) defect in graphene and calculated vibrational frequencies. We have encountered transition states with some small negative frequencies. Upon adjustingthe calculation

procedure, we were able to resolve the negative frequency issue, and therefore the simulation-predicted stability agrees with the experimental results[31]. The modification we made was simple; we manually displaced the atoms, which have negative eigenvalues.With this modification of the input, the structure achieved the stability. The structures before and after optimization are shown in Figure 3.7.

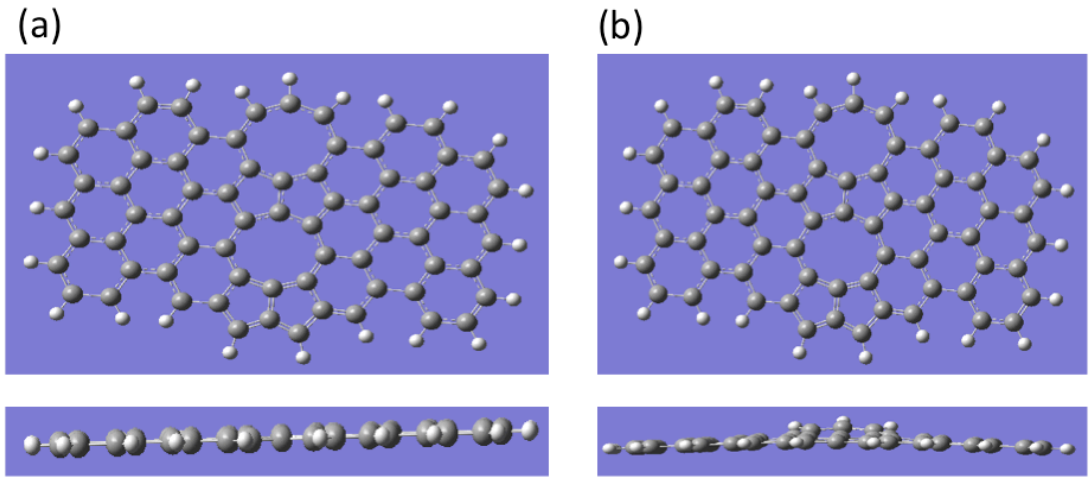

Figure 3.7(a) and (b) show the pentagonal-octagonal pair (POP) defectbefore and after optimization.

3.1.2.5 Flower Defect

According to theoretical studies any structure having pentagon and heptagon pair next to a hexagon is expected to have deformation in the graphene structure[45]. But when the pentagon and heptagon pairs are arranged next to each other in a circular manner, and next to hexagons, they will notcause any deformation in the structure[45]. Recently flower defect is observed experimentally and expects to open bouquet of possibilities

for different applications[32]. We have considered different types of flower defect. The optimized structures of different flower defects are represented inFigure 3.8.

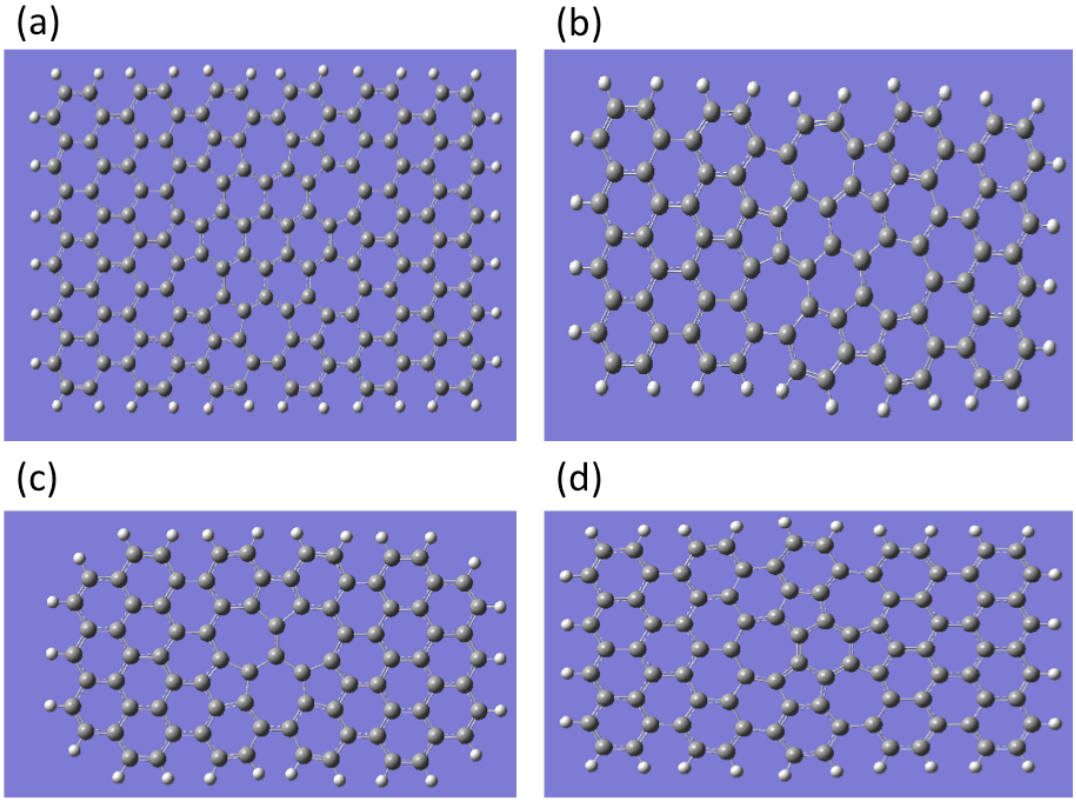

Figure 3.8Flower defect (FD): Experimentally observed structure FD1 (a) together with various other arrangements; FD2 (b), FD3 (c), FD4 (d) considered in our study.

Out of all the four different flower defects we have considered the flower defect in Figure 3.8 (a) is stable and experimentally observed. For remaining structures we have observed transition states with higher negative frequencies, which make the structure unstable.

3.1.3 Vibration Frequencies

We summarize the lowest ten vibration frequencies calculated for various defects considered in this work in Table 3.1. These frequencies are obtained by using method/basis B3LYP/6-31g that should provide reasonably accurate estimates. This assumption is further supported by comparing our results with previous experimental and theoretical studies, as explained in Section 3.1.2 above.

Vacancy	Adatom	A-V pair	SWD	ISWD	POP	Flower Defect 1	Flower Defect 2	Flower Defect 3	Flower Defect 4
-662.5	-504.9	13.837	4.1080	16.744	17.586	6.952	-60.57	-127.1	-114.5
-496.0	36.388	19.282	16.803	20.597	21.381	7.151	-19.91	-54.99	-105.0
-14.73	41.226	31.363	19.719	30.539	49.373	18.238	5.8124	-46.38	-22.72
-11.70	54.178	39.737	42.405	47.903	54.514	21.239	24.421	-25.88	-16.90
-5.877	63.562	41.058	49.121	55.235	70.766	27.578	26.464	-21.17	-7.958
15.855	75.342	54.863	55.151	57.581	79.342	35.140	36.258	41.456	24.797
25.023	93.033	58.840	62.463	61.867	82.827	36.431	45.339	42.898	27.998
43.928	97.384	74.145	69.557	69.749	89.948	48.409	57.533	61.590	49.169
50.108	97.845	79.336	80.190	81.000	109.99	57.368	69.454	69.564	72.509
56.43	101.16	84.961	85.866	90.554	123.49	57.937	81.210	93.857	73.918

Table 3.1: The lowest ten frequency values of each defect considered in this work, in units of cm^{-1}.

Based on the results presented in Table 3.1 we summarize the stability assessment results in Table 3.2. In Table 3.2, we also present results from previously published works if available.

Defect	Gaussian Results	Other results
Vacancy	Unstable	Unstable [29]
Adatom	Unstable	Unstable [29]
Vacancy-Adatom pair	Stable	Stable [29]
Stone Wales	Stable	Stable [29]
Inverse Stone Wales	Stable	----------
POP	Stable	Stable [11]
Flower Defect 1	Stable	Stable [12]
Flower Defect 2	Unstable	----------
Flower Defect 3	Unstable	----------
Flower Defect 4	Unstable	----------

Table 3.2: Stability assessment results for various defects based on the frequency calculation results presented in Table 3.1. Results from other published works, if available, are also included.

3.2 Raman Activity

Raman spectroscopy has a wide variety of applications from airport security and medicine to characterization of materials. Raman spectrum is like a fingerprint of the organic elements present in the given structure as Raman peaks in the spectrum varies with the type of bonds and the elements in the structure.

3.2.1 Raman Activity of Defected Graphene

In our research we have studied Raman activity of different structures with defects and compared them to the pristine graphene nanoflake to determine the unique Raman peaks that define the defect in the structure. We summarize the distinct Raman peaks found for the stable defects and the pristine cases in Table 3.3. To calculate the Raman intensity peaks, a utility program was written which will extract the data from a general frequency output. The results for the pristine case in Table 3.3 are obtained for a defectless nanoflake whose size is the same as that of the flake with Stone-Wales defect (Figure 3.4).

Pristine	Adatom-Vacancy	Stone-Wales	Inverse Stone-Wales	Pentagonal Octagonal Pair	Flower Defect 1
1126.39	1224.37	310.36	800.13	752.09	289.54
1150.6	1241.17	423.44	1109.52	1071.87	638.55

1226.5	1293.73	476.48	1136.99	1138.4	728.29
1251.70	1299.21	569.27	1223.07	1154.93	797.07
1272.33	1301.26	597.5	1301.09	1201.01	836.15
1296.43	1308.04	654.86	1323.47	1211.64	932.62
1312.04	1369.28	654.86	1346.90	1255.74	989.86
1318.6	1376.26	713.18	1350.99	1267.33	1031.96
1330	1398.05	893.88	1394.39	1302.25	1137.1
1348.9	1399.19	943.9	1403.68	1315.60	1149.53
1366.15	1404.11	970.86	1407.34	1376.84	1186.50
1380.76	1502.32	1061.83	1415.26	1384.45	1208.8
1397.97	1578.56	1184.51	1450.48	1386.72	1215.35
1407.15	1609.82	1376.71	1477.60	1399.46	1235.93
1420.16	1612.89	1406.53	1483.02	1401.71	1250.8
1453.08	1617.09	1451.82	1419.30	1422.08	1251.8
1505.24	1624.95	1457.81	1504.63	1447.27	1272.26
1559.42	1631.14	1617.04	1526.13	1527.00	1314.52
1612.80	1648.54	1755.40	1571.47	1552.27	1335.90
1623.21	1665.40	1779.12	1626.94	1605.21	1441.50
1640.85	3193.49	3376.25	1679.23	1647.14	1488.63
1656.63	3196.5	3412.67	3211.61	1682.73	1523.40
3213.63	3211.38	3433.35	3227.26	3210.92	1637.67

Table 3.3 Raman frequencies corresponding to the higher peaks in vibration spectra for pristine and stable defected graphene nanoflakes (cm^{-1}).

From theresults presented in Table 3.3 we note that Stone-Wales defect is characterized by several (~11) low-frequency peaks that are not neither present in the pristine case nor in the other defect cases. Inverse Stone-Wales and pentagonal-octagonal pair, each has one low-frequency peak that is not observed in the pristine

curve. Flower defect 1 has a few (~7) low frequency peaks that are not observed in the pristine case. Among the stable defect structures considered here, only the adatom-vacancy defect has frequencies that are comparable to and systematically (slightly) higher than the frequencies of the peaks for the pristine case. This analysis can help in interpreting the signatures of different stable defect types within the graphene lattice, based on Raman intensity results. Raman spectra of the pristine patch together with those of all the defects are shown in the Figures 3.9, 3.10, 3.11, 3.12, 3.13, and 3.14.

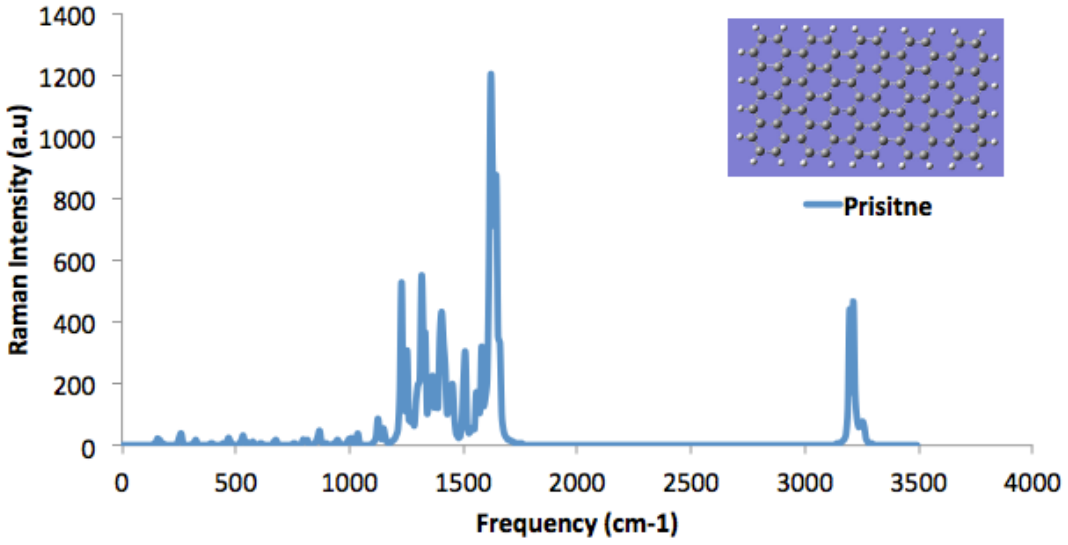

Figure 3.9L: Raman spectrum of the pristine patch. Atomc structure of the patch is shown in inset. The peak at 1600 cm^{-1} is graphene's G peak. D peak is located around 1350 cm^{-1}. The G-band is the only band coming from a normal first order Raman scattering process in graphene[42]. Finite size of the patch contribute to the presence of other peaks.

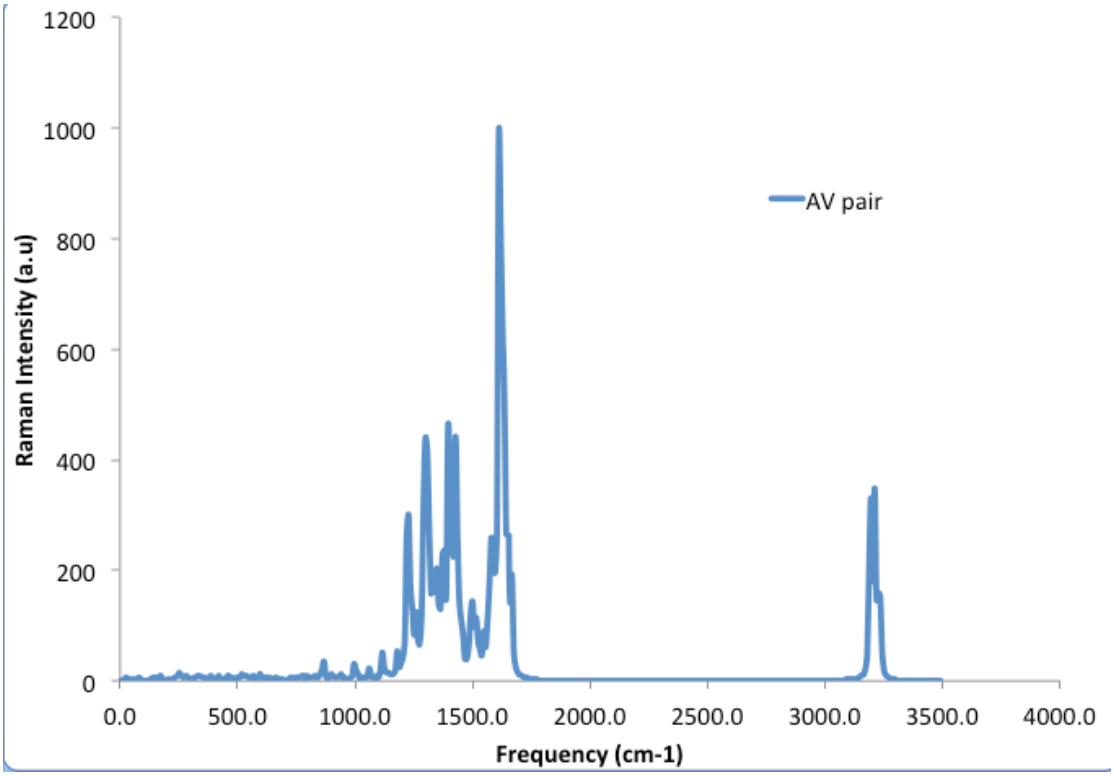

Figure 3.10: AV Raman spectrum.

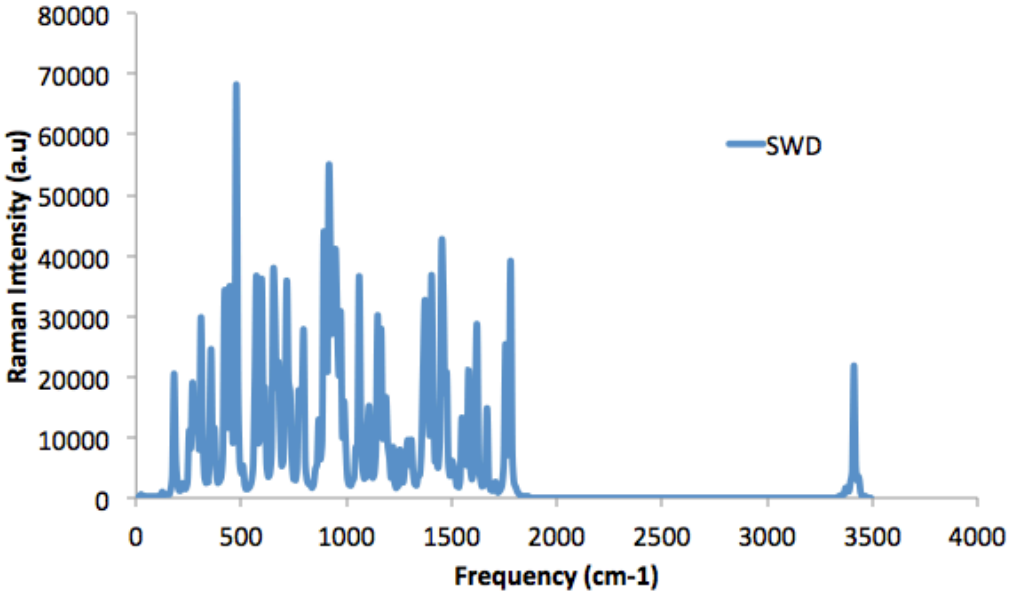

Figure 3.11: SWD Raman spectrum.

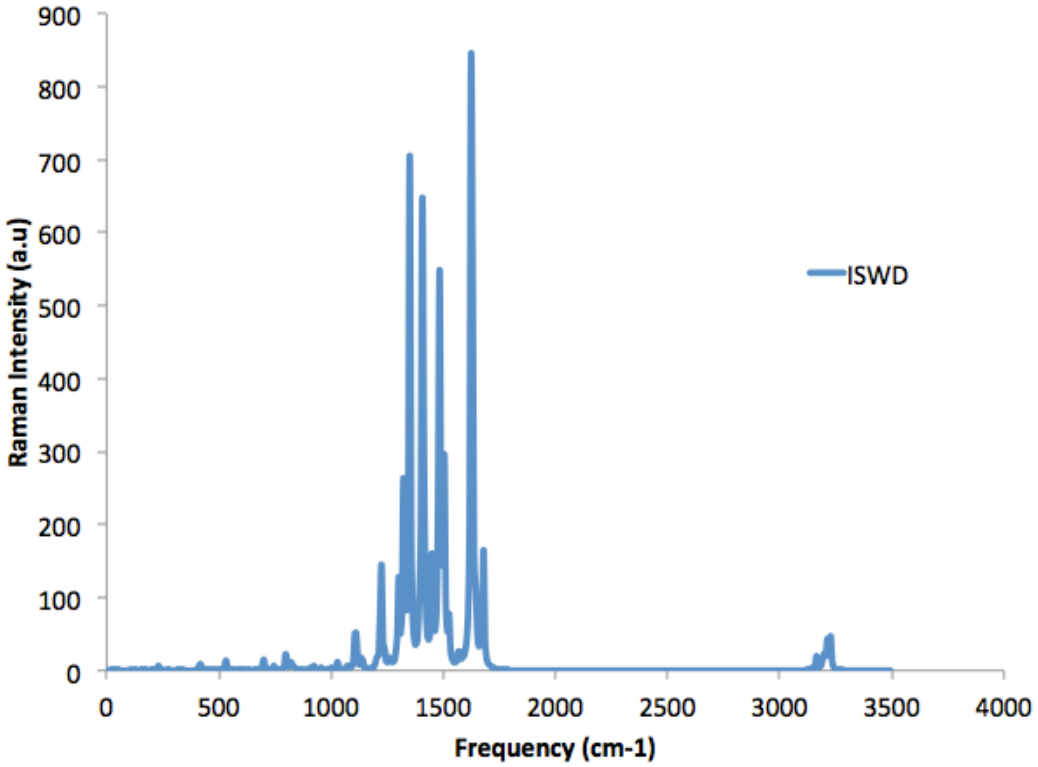

Figure 3.12 ISWD Raman spectrum

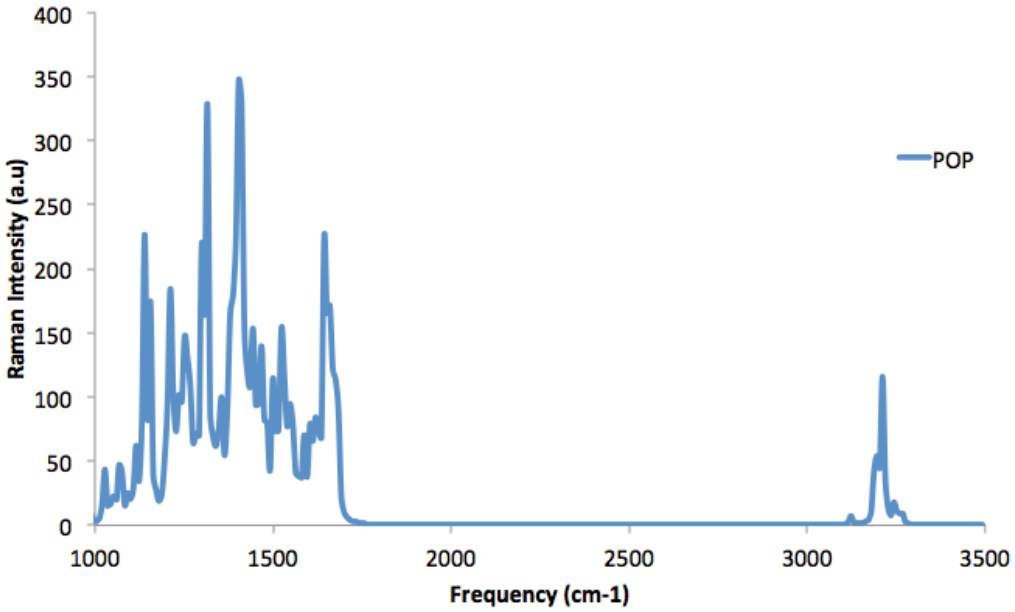

Figure 3.13 POP Raman spectrum

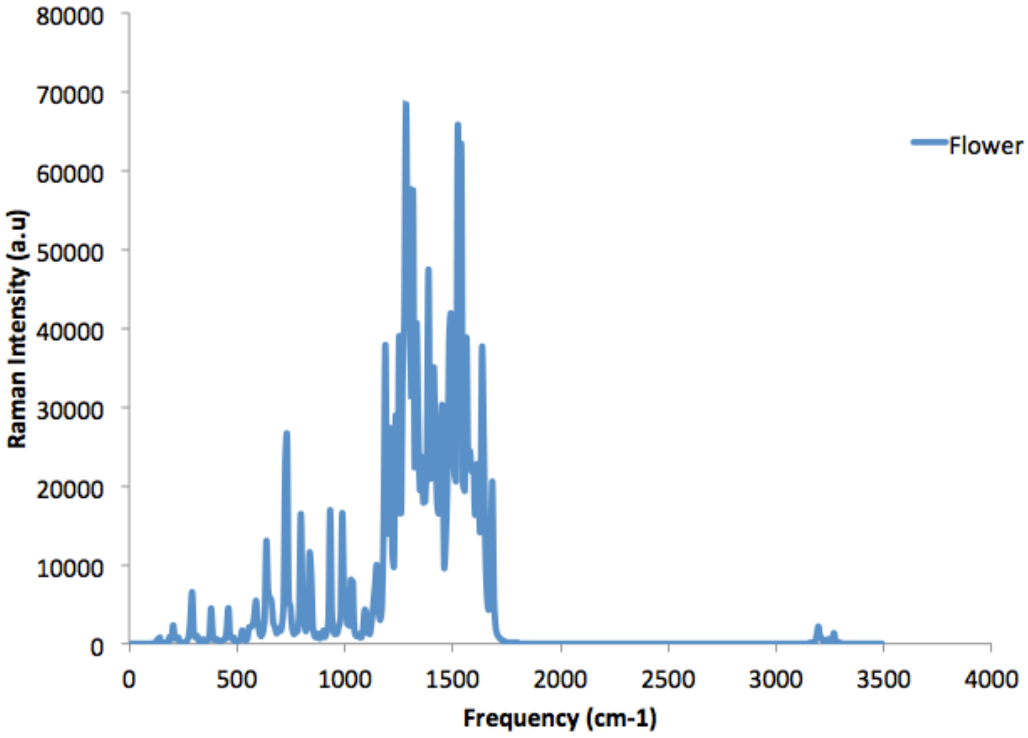

Figure 3.14 Flower defect Raman spectrum

3.2.2 Validation of the Raman Calculation Approach

In this section we discuss the validation of our Raman calculation approach using the results for C_{60} molecule. First we calculated the phonon frequencies of the C_{60} molecule using GAUSSIAN software. The reason for choosing C_{60} molecule is two-fold. First reason is that the computational time taken for the calculation is less compared to larger fullerene molecules and the second reason is the availability of phonon density of states of a single C_{60} molecule in the literature. We also compared the obtained frequency values from the GAUSSIAN output with the experimental values for single C_{60} molecule[61]. The results are summarized in Table 3.4.

Theoretical frequencies as obtained with ab initio Hartree−Fock are well-known to be consistently too high by about 10% or so[62],as compared with experiments due to neglect of electron correlation and anharmonicity. After calculating the frequency values we use the utility program to extract the data by assigning a Gaussian function to each frequency. Choice of proper Gaussian width plays an important role in validating our results. Raman spectrum and phonon density of states are similar, so we compared the peak values of the calculated Raman activity with the experimental values[63]. Taking the width of the Gaussian curve as 4 cm^{-1}, it is observed that our

results are generally in good agreement with experimental data (Table 3.4). Raman spectrum of C_{60} molecule is shown in the figure 3.15

C_{60} Raman modes Experimental results [64]	C_{60} Raman modes Theoretical results[65]	Our calculated phonon modes
270	272	292.889
430	427	482.657
493	547.6	499
708	552.4	764
772	779.8	805
1099	1160	1153.82
1248	1398	1275.7
1426	1688.2	1467.08
1468.5	1627.4	1515
1573	1830.7	1700

Table 3.4 Comparison of C_{60} Raman modes

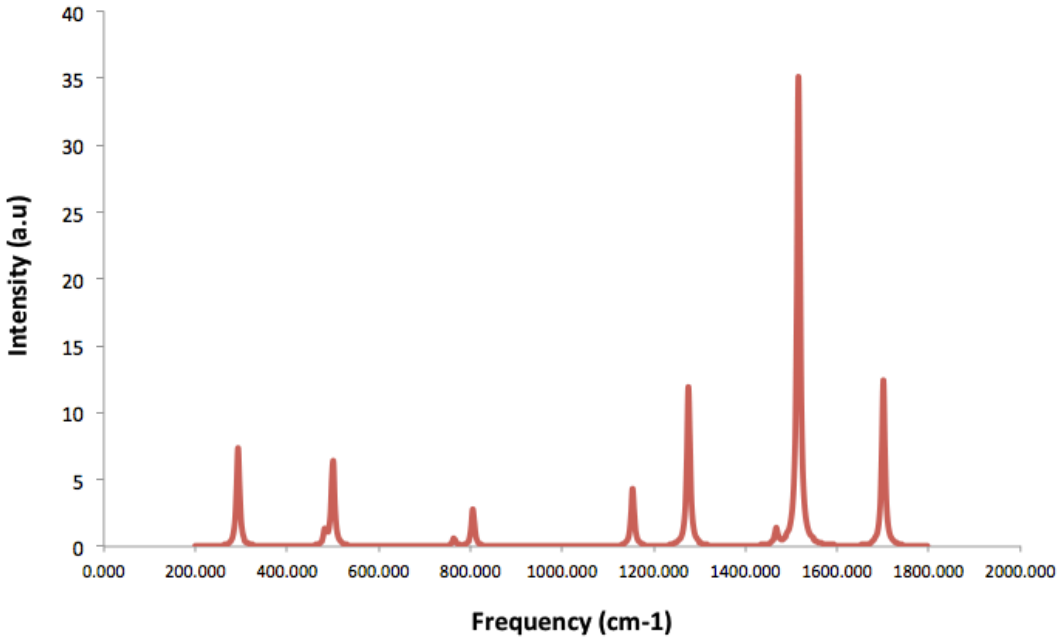

Figure 3.15 Raman spectrum of C_{60} molecule

3.3 Transport through Defected Graphene Nanoribbons

In this section we present the coherent transport calculation results of the graphene nanoribbon with different defects, which are found to be stable according to our calculations. Coherent transport of each stable defected structure is compared with the coherent transport through pristine graphene nanoribbon with the same geometrical width. In order to calculate conductance of defected GNRs, we first relax the whole structure is relaxed using Hartree-Fock method and 3-21g basis set. The relaxed structure is used to perform electronic structure calculations using BLYP method with 3-21g basis set. The output of the electronic calculation is taken as input data for the coherent transport calculations using TARABORD program[50].The Hamiltonian and overlap matrices of the defected central region of the GNRs are used together with the corresponding matrices for the pristine left and right contacts to calculate conductance through the structure. As such, we treat only one defect in each GNR.

Coherent transport calculation includes estimating the Fermi energy of the pristine GNRs. The calculated pristine GNR band gaps are compared with the band gaps of the pristine GNR with different widths reported by Son et al.[66].

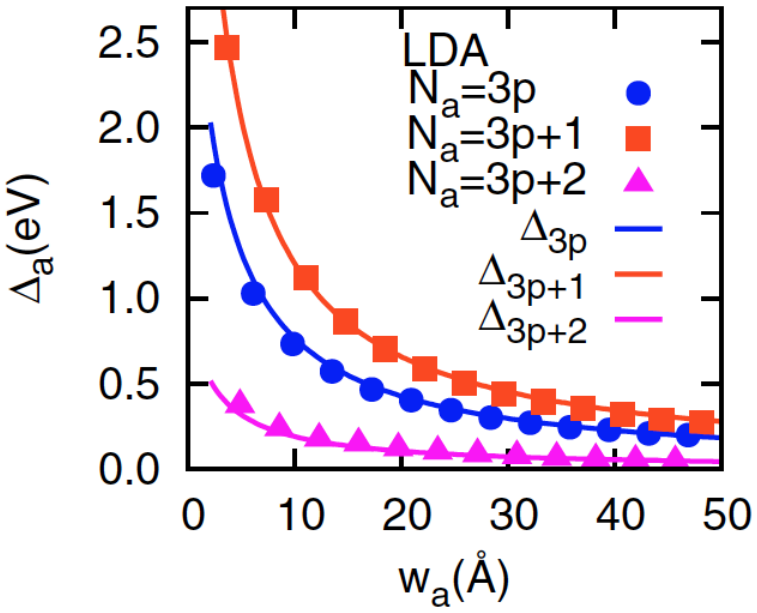

Figure 3.16 Variation of band gap of armchair graphene nanoribbons as a function of width (w_a) (Son et al [66]). N_a indicates the number of carbon chains across AGNR's witdth.

All the stable defected structures are considered for conductance calculations except for flower defect 1 that is too wide for calculating transport within a reasonable time.

3.3.1 Inverse Stone Wales Defect

For inverse Stone-Wales Defect (ISWD), we considered the structure shown in Figure 3.17, which has a molecular junction part shown in the red inset. It has left and right contacts of length 1.5 unit cells on both sides and also has additional layers which act as buffers preventing open boundary. We also considered the pristine GNR with the same width, which was shown in the Figure 3.18.

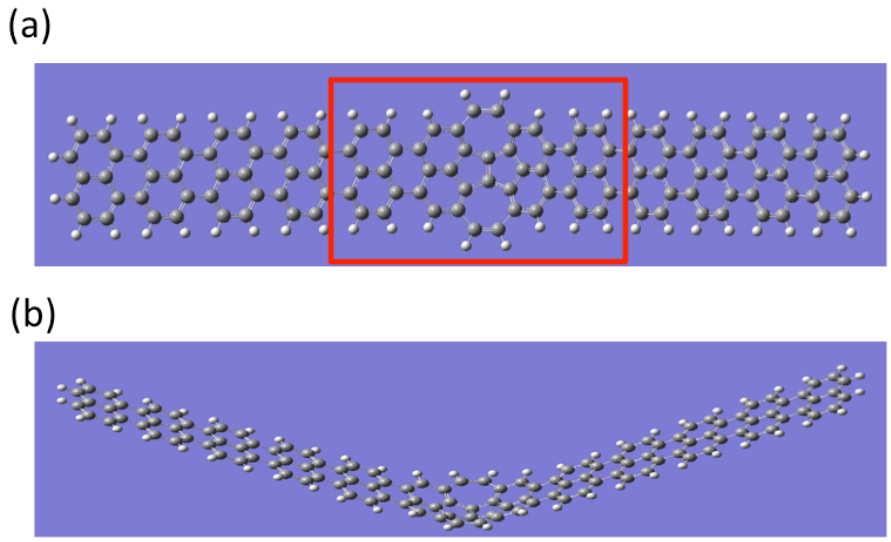

Figure 3.17: GNR with inverse Stone-Wales defect (ISWD) top (a) and side (b) views. Bending angle of this defected structure is 32°.

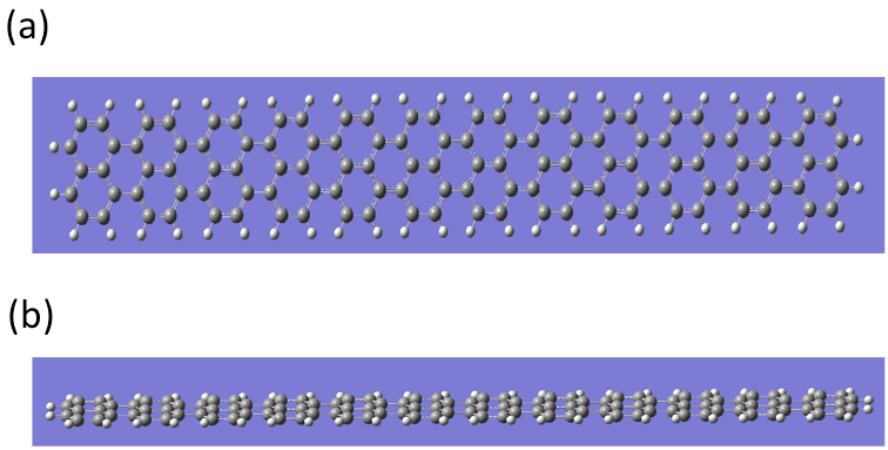

Figure 3.18 Pristine GNR with same width as that with INSWD top (a) and side (b) views.

From Figure 3.17 we observe that optimizing GNR with ISWD results in severe bending. Full-range and high-resolution conduction curve for pristine and INSWD are shown in Figures 3.19 and 3.20, respectively. We can see that the conduction of ISWD-GNR is less when compared to the pristine GNR. The width of the pristine

GNR in this case is 4.79Å and number of carbon chains is 5. These give the bandgap of approximately 0.4eV[66], according to a previous LDA study, and is in agreement with the result depicted in Figure 3.13. For ISWD-GNR we notice a band gap increase to around 3 eV which indicates significant disruption of transport upon introducing ISWD in such a narrow GNR.

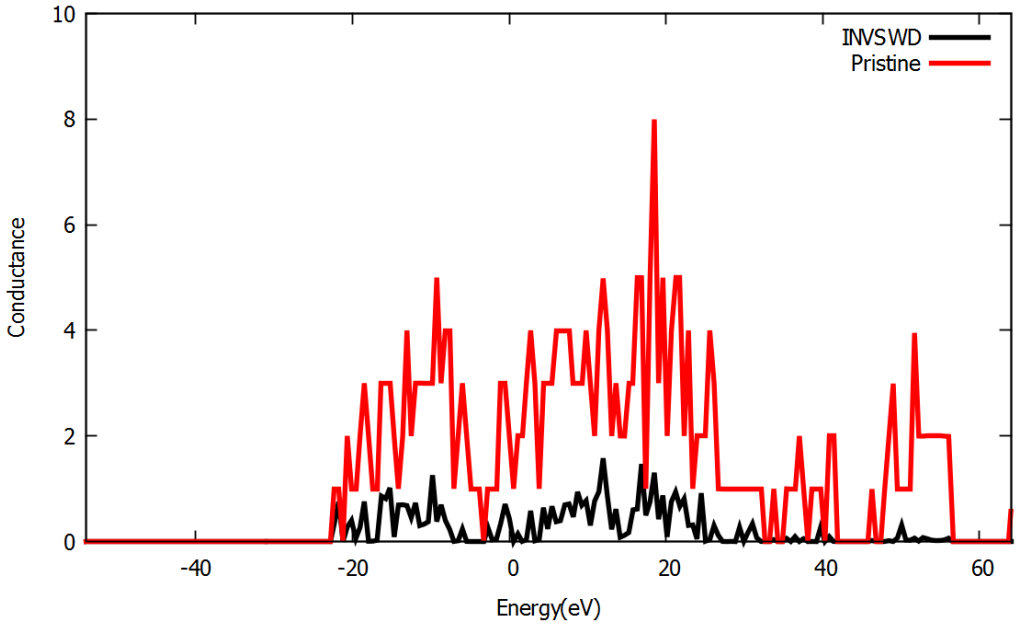

Figure 3.19 Conduction curve for ISWD and pristine GNR with full energy range.

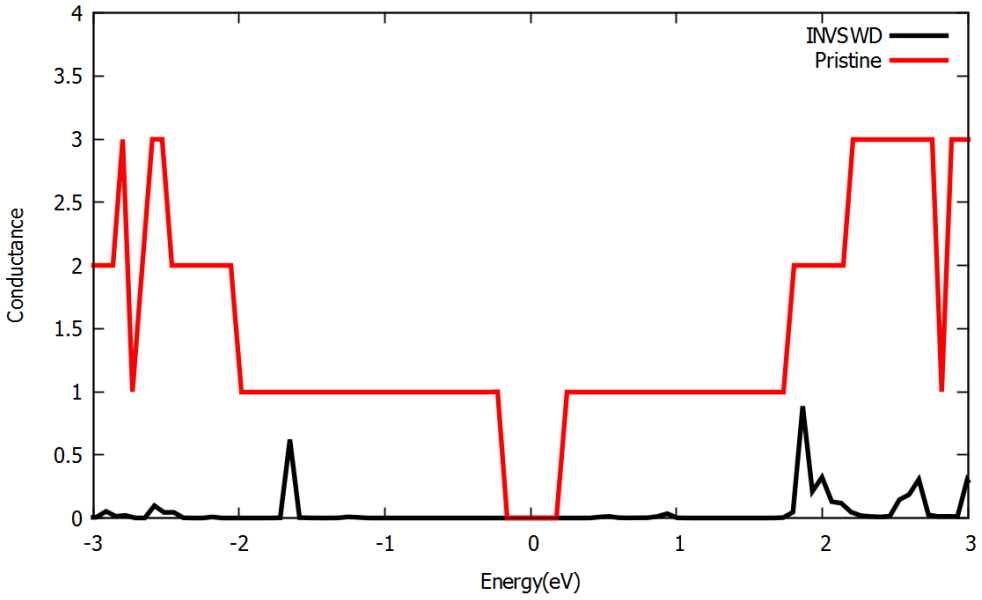

Figure 3.20 High-resolution conduction curves of ISWD and pristine GNR focused around Fermi energy (set to zero).

3.3.2 Stone Wales Defect

Stone Wales defect (SWD) is one of the stable defects whose stability results agree with the experimental results. For our calculations we considered the structure which has a molecular junction part shown in the red inset in figure 3.21.It has left and right contacts of 1.5 unit cells each on both sides and also has additional layers which act as a buffer. We considered the pristine GNR with the same width, which is shown in the Figure 3.22.

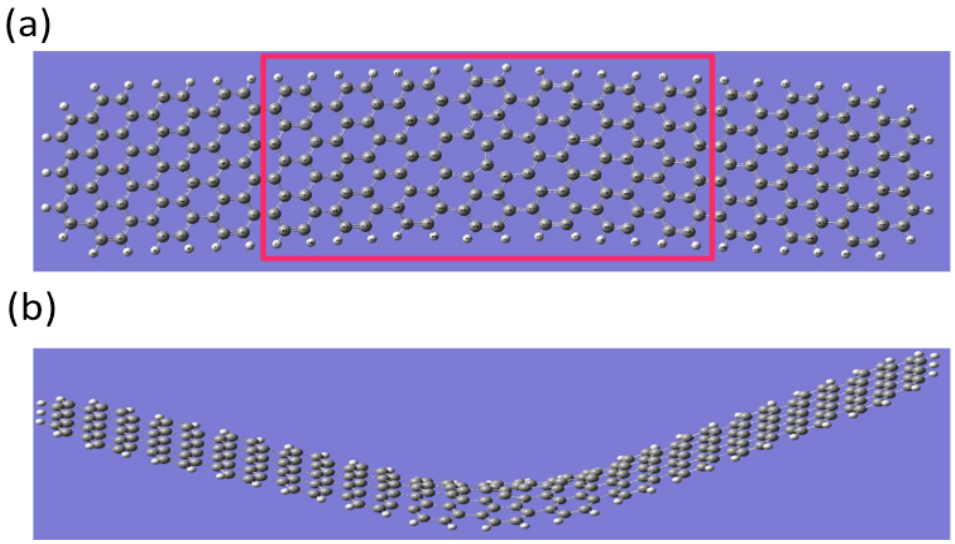

Figure 3.21: GNR with Stone-Wales defect top (a) and side (b) views. Bending angle of this defected structure is 29°.

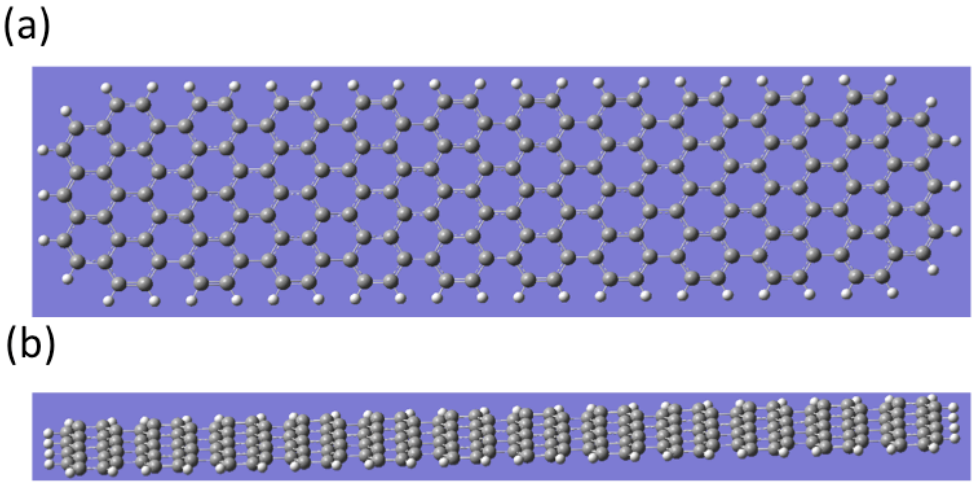

Figure 3.22 Pristine GNR of whose width is same as the ones with SW, AV, and POP defects; (a) top and (b) side views.

Full range conduction curves for SWD and pristine GND are shown in Figure 3.23. High-resolution conduction curves for both pristine and SWD near Fermi energy are shown in Figure 3.24. We can see that conduction of ISWD-GNR is less when

compared to the pristine GNR. Width of the pristine GNR in this case is 9.53Å and number of carbon chains is 9. Son et al. previous LDA work reports a band gap of approximately 0.75 eV [66] for such an armchair GNR, which agrees with the band gap from our calculation. Here also we notice a band gap increase upon introducing defect. The band gap increase, however, turns out to be less than that of ISWD-GNR, which is attributed to the narrower GNR in the latter case.

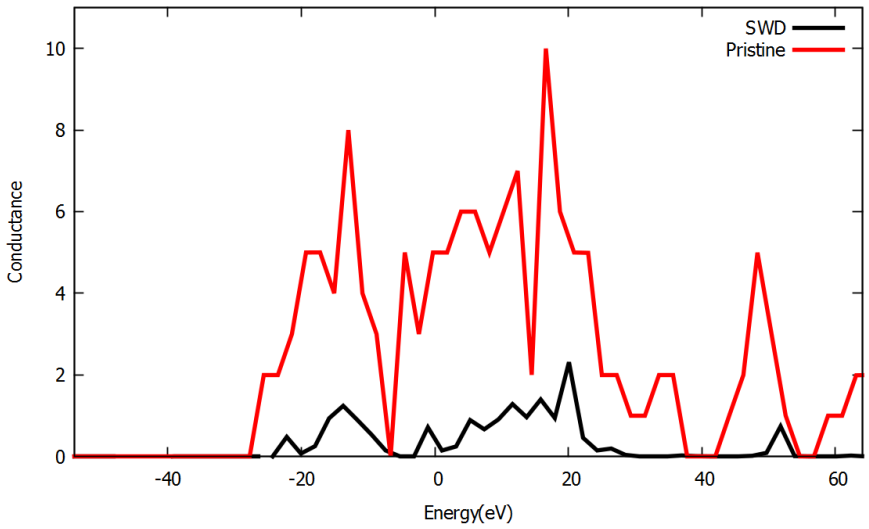

Figure 3.23: Full range conduction curve for pristine and SWD GNR.

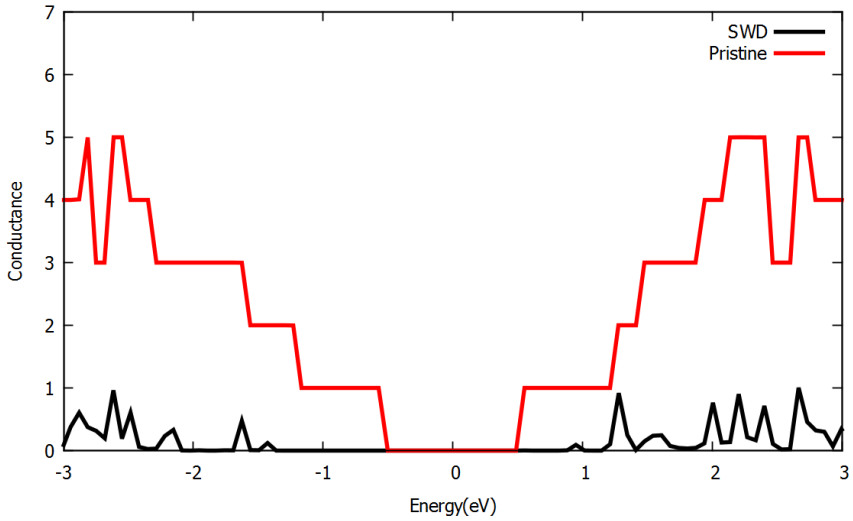

Figure 3.24: High-resolution conduction curve for SWD and Pristine GNR focused around Fermi energy (set to zero).

3.3.3 Adatom-Vacancy Pair Defect

Adatom-vacancy defect (AVD) is one of the stable defects whose stability results agree with the experimental results. For our calculations we considered the structure which has a molecular junction part shown in the red inset in Figure 3.25. It has left and right contacts of 1.5 unit cells each on both sides and also has additional layers which act as a buffer. We considered the Pristine GNR with the same width, which is shown in the Figure 3.22.

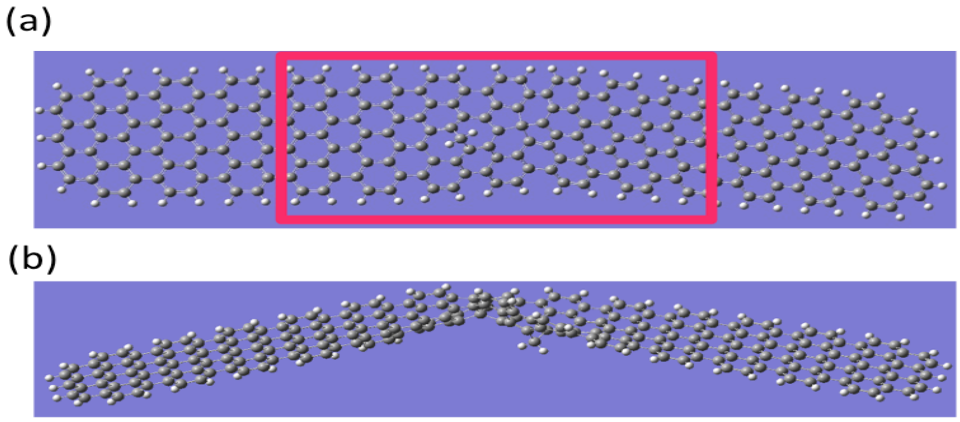

Figure 3.25: GNR withAdatom-vacancy defect top (a) and side (b) views. Owing to structure twist, bending angle is not well-defined, unlike the other cases.

Full range and high-resolution conduction curves are plotted for the AVD and pristine GNR in Figures 3.26 and 3.27, respectively.

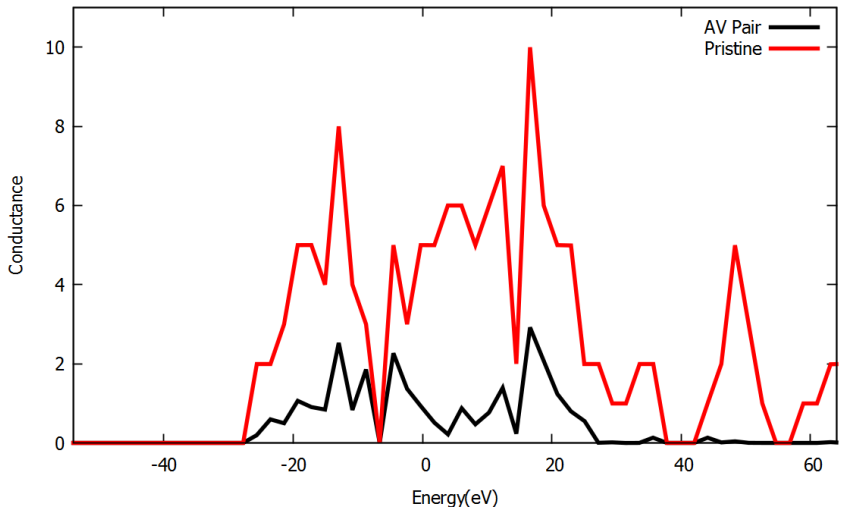

Figure 3.26: Full range conduction curves for AVD and pristine GNR.

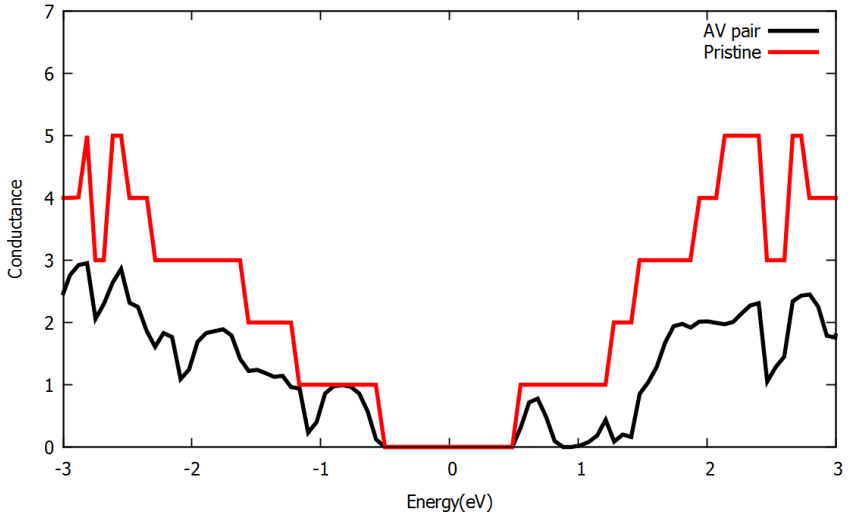

Figure 3.27: High resolution conduction for AVD and pristine GNR focused around the Fermi energy (set to zero).

The conductance curves for AVD specially the high-resolution one depicted in Figure 3.27 represents an interesting result in which the band gap of pristine remains nearly intact upon introducing AVD. In other words, AVD results in least amount of transport disruption among the defects considered in this work.

3.3.4 Pentagonal-Octagonal Pair Defect

The pentagonal-octagonal pair defect (POPD) is inserted within GNR similar to the cases for SW and AV defects. The structure of the central junction after optimization is depicted in Figure 3.28.

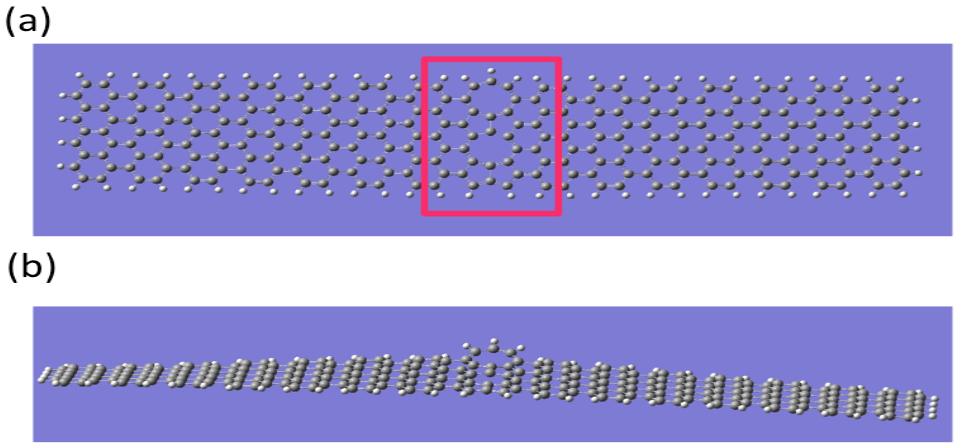

Figure 3.28: GNR with pentagonal-octagonal pair defect top (a) and side (b) views. Bending angle of this defected structure is 18°.

Figure 3.28 represents the least amount of bending among the defects considered. Another important characteristic of POPD is the presence of a single hydrogen atom within the junction region. The corresponding unpaired electron causes this defect to act differently for carriers with spins up and down.

Figures 3.29 and 3.30 depict full-range and high-resolution conductance results, respectively. We notice that POPD results in a small amount of gap increase for both

spin orientations. Furthermore, slight but nevertheless noticeable differences exist in the conductance characteristics of the two spin orientations (alpha and beta), e.g., around +1 and -1 eV. This unique property of POPD can be used in spintronics applications, as within some specific energy range one spin orientation is blocked while the other is allowed to pass through.

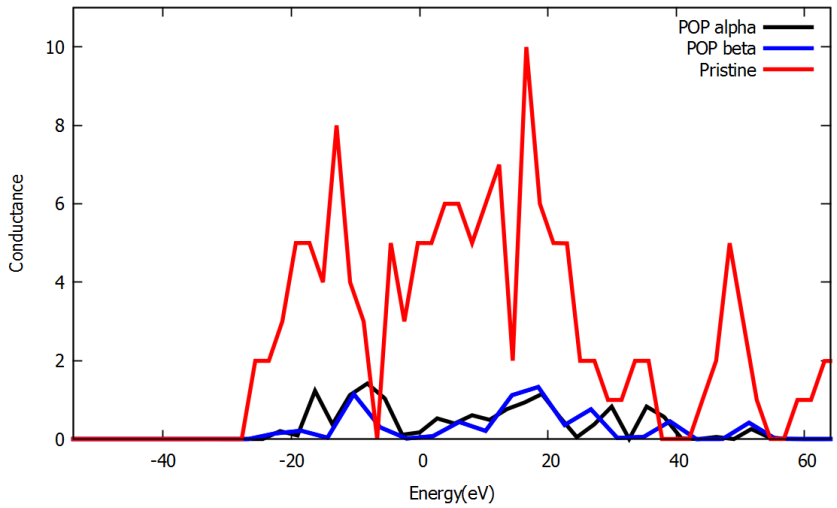

Figure 3.29: Full range conductance curves for POPD and pristine GNR. Different spin orientations of charge carriers are represented by alpha and beta.

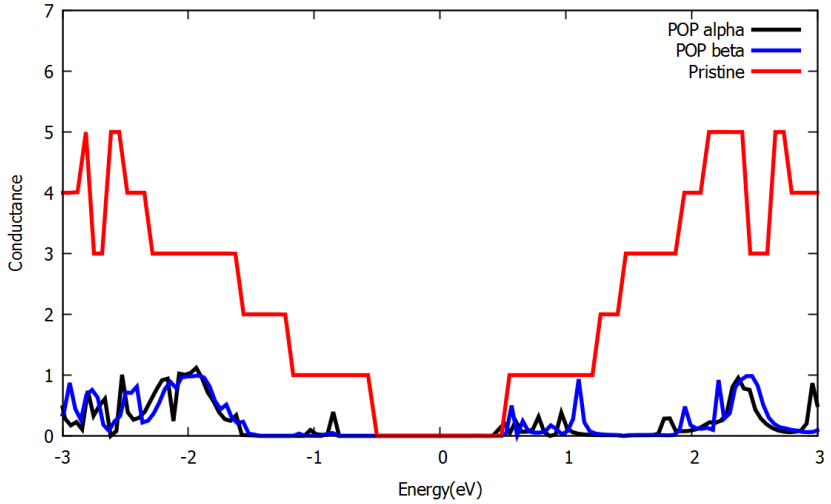

Figure 3.30: High resolution conductance curves for POPD and pristine GNR focused around Fermi energy (set to zero). Different spin orientations of charge carriers are

represented by alpha and beta.

4. Conclusions:

We investigated the characteristics and stability of various defects which are possible in graphene lattice. Using accurate density functional theory relaxation and frequency calculations, we found that vacancy and adatom defects are both unstable, while adatom-vacancy pair, as well as Stone-Wales, inverse-Stone-Wales, pentagonal-octagonal pair, and one type of flower defects, are all stable and can happen in graphene lattice. The stability assessments in this study were compared to the available results in the literature. In particular, we found that negative vibration frequency results that we obtained for some defects in graphene nanoflakes correspond to structures, which were experimentally determined to be unstable.

We further characterized the stable defects via simulating their vibrational and Raman responses, and found that their Raman activities are different from one another and from that of the pristine graphene.

Next, we investigated the changes that occur to the transport characteristics of graphene nanoribbons (GNR) upon introducing various stable defects. As a required

step, we obtained the ab initio optimized structures of GNRs with various defects that generally resulted in severe bending. Subsequent conductance calculations revealed that the amount of band gap increase depends on the type of defect: While inverse Stone-Wales and Stone-Wales defects significantly increase the band gap, adatom-vacancy defect almost leaves the band gap intact. Pentagonal-octagonal pair defect increases the gap only slightly, and has the unique character of spin-polarization owing to an unpaired electron, and can disrupt different spin orientations in different ways.

The results of this study clarify GNR characteristics under realistic condition of defected structures. The rusts are also important as they show how (intentional) defect generation can help in engineering GNRs transport properties, such as conductance value for different spin orientations and band gaps, with possible applications in nanoelectronics and spintronics.

5. References:

1) World of Carbon – Interactive Nano-visualization in Science & Engineering Edukation (IN-VSEE)". Retrieved 2008-10-09 from wikipedia of Carbon.

2) Andre K Geim and Philip Kim. *Carbon Wonderland*, Scientific American Magazine , March 17-2008.

3) B. Z. Jang and W. C. Huang,"Nano-scaled Graphene Plates," US Patent Application No. 10/274,473 (submitted on 10/21/2002); now U.S. Pat. No. 7,071,258 (issued 07/04/2006).

4) A. H. Castro Neto, F. Guinea, and N. M. R. Peres, Physics World, November 2006.

5) A.K.Geim and K.S.Novoselov. "*The rise of Graphene", Nature* **6** , 183-191 (2007).

6) D.V. Kosynkin, A L. Higginbotham, A.Sinitskii, Jay R. Lomeda, A.Dimiev, "*Longitudinal Unzipping of Carbon Nanotubes to form graphene nanoribbons*," Nature **458**, 872-876 (2009).

7) Liying Jiao, Xinran Wang, Georgi Diankov, Hailiang Wang, Hongjie Dai: "*Facile synthesis of high – quality graphene nanoribbons"* .nnano:**5**,321 (2010).

8) Olga V. Pupysheva, Amir A.Farajian, Cory R.Knick, Aruna Zhamu and Bor Z.Jang. "*Modeling Direct Exfoliation of Nanoscale Graphene Platelets"*, J.Phys. Chem.C, **114**, 21083-21087 (2011).

9) Frank J.Owens (2008). "*Electronic and Magnetic Properties of Arm chair and Zigzag graphene Nanoribbons"*. The Journal of Chemical Physics, **128**,194701(2008).

10) Kuzmenko, A.B.; Van Heumen, E.: Carbone,F.; Van der Marel, D *Universal Infrared Conductance of Graphite*. PhyRevLett **100**,117401 (2008.)

11) Lee,C.et.al *"Measurement of the Elastic Properties and Intrinsic Strength of Monolayer Graphene"* Science **321**,385-388 (2008).

12) K.Sasaki, S.Murakami, R.Saito "*Stabilization mechanism of edge states in graphene*". Appl.Phys.Lett.**88,** 113110 (2006).

13) M.Fujita, K.Wakabayashi,K.Nakada and K.Kusakabe "*Peculiar Localized state at Zigzag Graphite Edge*" J.Phys.Soc.Jpn.**65**,1920 (1996).

14) Schedin F,A.K.Geim,V.Morozov,E.W.Hill,P.Blake et.al. "*Detection of individual gas molecules adsorbed on graphene*". Nature. Mater.**6** 652 (2007).

15) Ponomarneko L A. Gorbachev RV, MAyorov AS,Abanin DA et.al. "*Giant nonlocality near the Dirac point in graphene*", Science **320** 356 (2008).

16) Hill E W, A.K.Geim, P.Blake, K.Novoselov, F.Schedin**"***Graphene Spin Valve Devices"* IEEE Trans Magn. **42** 2694 (2006).

17) Blake P et.al. "*Graphene-Based Liquid Crystal Device"*Nano Lett.**8**, 1704 (2008).

18) V Tozzini and V Pellegrini "*Reversible Hydrogen storage by controlled buckling of Graphene Layers".* J. Phys. Chem. C. **115,** 25523 (2011).

19) Yanan Tang, Zongxian Yang and Xianqi Dai. "*Trapping of metal atoms in the defects on graphene ".* J.Chem. Phys. **135**, 224704 (2011).

20) F.Schedin, A.K. Geim, S.V. Morozov, E.W.Hill, P.Blake, M.I. Katasnelson & K.S. Novoselov, "*Detection of individual gas molecules absorbed on graphene*." Nature Mater.**6,** 652 (2007).

21) Sergey Rumyantsev, Guanxiong Liu, Michael S. Shur, Radislav A. Potyrailo, and Alexander A. Balandin , "*Selective Gas Sensing with a Single Pristine Graphene Transistor"*. Nano Lett.**12,** 2294 (2012).

22) G.Ko, H.Y.Kim, J.Ahn, Y.M Park, Y.Lee, J.Kim, "*Graphene-based nitrogen dioxide gas sensors".* Current App.Phys.**10**, 1002 (2010).

23) Y. C. Cheng, Z. Y. Zhu and U. Schwingenschlögl, "*Mechanical failure of zigzag graphene nanoribbons under tensile strain induced by edge reconstruction"*.J. Mater.Chem**.22**, 24676 (2012).

24) H.Zhang, G.Lee, K.Cho , "*Thermal transport in graphene and effects of vacancy defects"*. Phys.Rev.B.**84,**115460 (2011).

25) Narjes Gorjizadeh, Amir A Farajian and Yoshiyuki Kawazoe, "*The effects of defects on the conductance of graphene nanoribbons*" Nanotechnology**20,** 015201 (2009).

26) Meyer, J.C.; Kisielowski, C.; Erni, R.; Ro"ssell, M.D.; Crommie,M.F.;Zettl,A. "*Direct Imaging of Lattice Atoms and Topological Defects in Graphene Membranes".* Nano Lett. **8**, 3582-3586 (2008).

27) Ugeda M M; Brihuega I; Guinea F; Gomez-Rodriguez J M, "*Missing atom as a source of carbon magnetism* **".**Phys.Rev.Lett. **104 ,** 096804 (2010).

28) Florian Banhart, Jani Kotakoski and Arkady V. Krasheninnikov .“*Structural Defects in Graphene”*ACS Nano,**5**, 26–41 (2011).
29) Mauter, M. et al (2008). "Environmental Applications of Carbon-Based Nanomaterials.". *Environmental Science and Technology***42**: 5843–5859.37
30) Mark T.Lusk, David T. Wu and Lincoln D. Carr, “*Graphene Nanoengineering and the Inverse Stone Thrower Wales Defect”*. PhyRevB.**81**.155444 (2009).
31) Jayeeta Lahiri, You Lin, Pinar Bozkurt, Ivan I. Oleynik and Matthias Batzill, “*An extended defect in graphene as a metallic wire*,”Nature. Nano. **5**, 326 - 329 (2010).
32) E. Cockayne, G. Rutter, N. Guisinger, J. Crain, P. First and J. Stroscio. *“Grain boundary loops in graphene”.* Phys.Rev.B.**83**, 195425 (2011).
33) McMullan, D "Von Ardenne and the scanning electron microscope". *Proc Roy Microsc Soc***23**: 283–288 (1988).
34) Crewe, Albert V; Isaacson, M. and Johnson, D. (1969). "A Simple Scanning Electron Microscope". *Rev. Sci. Inst.***40** : 241–246 (1969).
35) F. T. Thema, M. J. Moloto, E. D. Dikio, et al., “Synthesis and Characterization Graphene Thin Films by Chemical Reduction of Exfoliated and Intercalated Graphite Oxide,” Journal of Chemistry, vol. 2013, Article ID 150536, 6 pages, 2013.
36) Greenough G.B; “Quantitative X-ray diffraction observations on strained metal aggregates”. *Proc. Metal. Phys.,* **3**: 176-219 (1952).
37) Lang, K.M.; D. A. Hite, R. W. Simmonds, R. McDermott, D. P. Pappas, and John M. Martinis (2004). "Conducting atomic force microscopy for nanoscale tunnel barrier characterization". *Review of Scientific Instruments***75**: 2726–273138)
38) L.Y.Meng and S.J.Park ,“Preparation and characterization of reduced graphene nanosheets via pre-exfoliation of graphite flakes”.Bull.Korean Chem.Soc.**33**, 209 (2012).
39) Joseph Goldstein (2003). *Scanning Electron Microscopy and X-Ray Microanalysis*. Springer. ISBN 978-0-306-47292-3. Retrieved 26 May 2012.
40) A.B.Kuzmenko, E.van Heumen, D.van der Marel “*Infrared spectroscopy of electronic bands in bilayer graphene”*.Phy.Rev.B.**79,**115441 (2009).
41) Kai M. Siegbahn - Nobel Lecture: Electron Spectroscopy for Atoms, Molecules and Condensed Matter". Nobelprize.org. 20 Dec 2012.
42) L.M.Malard, M.A.Pimenta, G.Dresselhaus, M.S.Dresselhaus ,“*Raman spectroscopy in graphene”.* Phys. Rep.**473**, 51 (2009).

43) Turner, D. W.; Jobory, M. I. Al "Determination of Ionization Potentials by Photoelectron Energy Measurement". J. Chem. Phys. **37** (12): 3007(1962).

44) M.C.Payne, M.P.Teter, D.C.Allan, T.A.Arias and J.D.Joannopoulos, "*Iterative minimization techniques for Ab-initio energy calculations: molecular dynamics and conjugate gradients"*. Rev. Mod. Phys. **64**, 1045–1097 (1992).

45) Mark T. Lusk and L.D.Carr , "*Nanoengineering Defect Structures on Graphene*": PhyRevLett **100**,175503 (2008).

46) Landauer R "*Quantum Graphs: an introductory study and brief survey"* Phil. Mag**.21**,863 (1970).

47) Pastawski H M "*Classical and quantum transport from generalized Landauer-Büttiker equations"*.Phys. Rev. B **44** 6329 (1991).

48) Tian W, Datta S, Hong S, Reifenberger R, Henderson J I and Kubiak C P "*Conductance spectra of molecular wires"* J. Chem. Phys. **109** 2874(1998).

49) Amir A Farajian, Rodion V Belosludov, Hiroshi Mizuseki, Yoshiyuki Kawazoe: "A general-purpose approach for calculating transport in contact–molecule–contact systems: TARABORD implementation and application to a polythiophene-based nanodevice"Thin Solid Films **499** (2006) 269 – 274.

50) Transport in Persian Developed by Dr.Amir A Farajian.

51) M.P. Lo´pez Sancho, J.M. Lo´pez Sancho, J. Rubio,"*Quick iterative scheme for the calculation of transfer matrices"* :J.Phys.F: Metal Physics **14** 1205 (1984).

52) R.Landauer. "Electrical resistance of disordered one dimensional lattices", Philos.Mag.**21**,863 (1970).

53)Gaussian 09, Revision **A.1**, M. J. Frisch, G. W. Trucks, H. B. Schlegel, G. E. Scuseria, M. A. Robb, J. R. Cheeseman, G. Scalmani, V. Barone, B. Mennucci, G. A. Petersson, H. Nakatsuji, M. Caricato, X. Li, H. P. Hratchian, A. F. Izmaylov, J. Bloino, G. Zheng, J. L. Sonnenberg, M. Hada, M. Ehara, K. Toyota, R. Fukuda, J. Hasegawa, M. Ishida, T. Nakajima, Y. Honda, O. Kitao, H. Nakai, T. Vreven, J. A. Montgomery, Jr., J. E. Peralta, F. Ogliaro, M. Bearpark, J. J. Heyd, E. Brothers, K. N. Kudin, V. N. Staroverov, R. Kobayashi, J. Normand, K. Raghavachari, A. Rendell, J. C. Burant, S. S. Iyengar, J. Tomasi, M. Cossi, N. Rega, J. M. Millam, M. Klene, J. E. Knox, J. B. Cross, V. Bakken, C. Adamo, J. Jaramillo, R. Gomperts, R. E. Stratmann, O. Yazyev, A. J. Austin, R. Cammi, C. Pomelli, J. W. Ochterski, R. L. Martin, K. Morokuma, V. G. Zakrzewski, G. A. Voth, P. Salvador, J. J. Dannenberg, S.

Dapprich, A. D. Daniels, Ö. Farkas, J. B. Foresman, J. V. Ortiz, J. Cioslowski, and D. J. Fox, Gaussian, Inc., Wallingford CT, 2009

54) Ji, M.; Liu, Z.F.;Gong, X.G. *BLYP in Molecules and Solids: "A Comparative Study with LDA and GGA*": American Physical Society, Annual APS March Meeting, March 18 - 22, 2002.

55) Elena E. Zvereva, Artur R. Shagidullin, and Sergey A. Katsyuba, "*Ab Initio and DFT predictions of Infrared Intensities and Raman activites.*."J. Phys. Chem.A.**115**, 63–69 (2011).

56) Gardeneir , D.J. *Practical Raman Spectroscopy* .SpringeVerlag, ISBN 978-0-387-50254-0.

57) Ayako Hashimoto, Kazu Suenaga, Alexandre Gloter, Koki Urita & Sumio iIjima, "*Direct evidence for atomic defects in graphene layer "*:Nature **430**, 870-873(2004).

58) Mark T. Lusk and L.D.Carr , *Nanoengineering "Defect Structures on Graphene"* : PhyRevLett **100**,175503 (2008).

59) Jie Ma, Dario Alfe , Angelos Michaelides and Enge Wang, "*Stone-Wales defects in graphene and other planar sp2 - bonded materials*:" PhysRevB**.80**.033407 (2009) .

60) Ibolya Zsoldos "*Effects of topological defects on graphene"* Nanotechnology, Science and Applications **3** 101–106(2010).

61) Vincenzo Schettino, Marco Pagliai, Lucia Ciabini and Gianni Cardini. "*The Vibrational Spectrum of Fullerene C_{60}"*: J.Phys.Chem.A, **105**,11192 (2001).

62) Cheol H.Choi and Miklos Kertesz: "*Vibrational Assignment of all 46 Fundamentals of C_{60} and C_{60}^{-6} : Scaled quantum mechanical results performed in redundant internal coordinates and compared to experiments*". J.Phys.Chem.A, **104**, 102 (2000).

63) Jose Menendez and John.B.Page*." Vibrational Spectrum of C_{60}.*"

64) Ping Zhou, Kai-An Wang, Ying Wang, and P.C. "Eklund. *Raman scattering in C60 and alkali-metal-saturated C60* **"**: Phys.Rev.B. **46**,2595 (1992).

65)Z.C.Wu, D.A.Jelski and T.F.George "*Vibrational motions of buckminsterfullerene*".**137,**291 (1987).

66) Young.W.Son, Marvin L.Cohen, Steven.G.Louie. "*Energy Gaps in Graphene Nanoribbons".*Phys.Rev.Lett. **97**, 216803 (2006).

67) M.Nagase, H.Hibino, H.Kageshima and H.Yamaguchi. "Local conductance measurement of few - layers of graphene on SiC substrate using an integrated nanogap probe ", J.Phys:Conf.Ser.100, 052006 (2008).